

AD \_\_\_\_\_

Award Number: ÜÎFVÜÒË€ÏËFË€€GF

TITLE: Ø↑\*ã~{↔^&ÁÓá´ ¨ãÁÆæ\æ´\↔~^Áá^äÁÆ~bæÁÓàà↔´↔æ´´]Á↔^Á  
 Ææä↔´ á\¨äÁÑãæáb\ÁÓá´ ¨ãÁÓÚ

PRINCIPAL INVESTIGATOR:  $\tilde{O} \mid \wedge \& \mid \sim \acute{A} \tilde{N} \leftrightarrow \acute{a} \wedge$

[illegible]

REPORT DATE: 06/15/2023

TYPE OF REPORT: N^{\wedge}|\acute{a}\rightarrow\acute{A}U|\uparrow\uparrow\acute{a}\tilde{a}]

PREPARED FOR: U.S. Army Medical Research and Materiel Command  
Fort Detrick, Maryland 21702-5012

DISTRIBUTION STATEMENT:

Approved for public release; distribution unlimited

The views, opinions and/or findings contained in this report are those of the author(s) and should not be construed as an official Department of the Army position, policy or decision unless so designated by other documentation.

<b>REPORT DOCUMENTATION PAGE</b>				Form Approved OMB No. 0704-0188	
Public reporting burden for this collection of information is estimated to average 1 hour per response, including the time for reviewing instructions, searching existing data sources, gathering and maintaining the data needed, and completing and reviewing this collection of information. Send comments regarding this burden estimate or any other aspect of this collection of information, including suggestions for reducing this burden to Department of Defense, Washington Headquarters Services, Directorate for Information Operations and Reports (0704-0188), 1215 Jefferson Davis Highway, Suite 1204, Arlington, VA 22202-4302. Respondents should be aware that notwithstanding any other provision of law, no person shall be subject to any penalty for failing to comply with a collection of information if it does not display a currently valid OMB control number. <b>PLEASE DO NOT RETURN YOUR FORM TO THE ABOVE ADDRESS.</b>					
<b>1. REPORT DATE (DD-MM-YYYY)</b> 01-02-2011		<b>2. REPORT TYPE</b> Annual Summary		<b>3. DATES COVERED (From - To)</b> 26 Jan 2010 - 25 Jan 2011	
<b>4. TITLE AND SUBTITLE</b> Improving Cancer Detection and Dose Efficiency in Dedicated Breast Cancer CT				<b>5a. CONTRACT NUMBER</b>	
				<b>5b. GRANT NUMBER</b> W81XWH-09-1-0021	
				<b>5c. PROGRAM ELEMENT NUMBER</b>	
<b>6. AUTHOR(S)</b> Junguo Bian  E-Mail: junguo@uchicago.edu				<b>5d. PROJECT NUMBER</b>	
				<b>5e. TASK NUMBER</b>	
				<b>5f. WORK UNIT NUMBER</b>	
<b>7. PERFORMING ORGANIZATION NAME(S) AND ADDRESS(ES)</b> The University of Chicago Chicago, IL 60637				<b>8. PERFORMING ORGANIZATION REPORT NUMBER</b>	
<b>9. SPONSORING / MONITORING AGENCY NAME(S) AND ADDRESS(ES)</b> U.S. Army Medical Research and Materiel Command Fort Detrick, Maryland 21702-5012				<b>10. SPONSOR/MONITOR'S ACRONYM(S)</b>	
				<b>11. SPONSOR/MONITOR'S REPORT NUMBER(S)</b>	
<b>12. DISTRIBUTION / AVAILABILITY STATEMENT</b> Approved for Public Release; Distribution Unlimited					
<b>13. SUPPLEMENTARY NOTES</b>					
<b>14. ABSTRACT</b> Breast cancer is the second leading cause of cancer mortality among women in the United States. Dedicated breast computed tomography (CT) has been developed for potential use as an imaging tool for breast-cancer screening or diagnosis, because it can yield three-dimensional(3D) volumetric images of the breast, thus overcoming inherent limitations of conventional two-dimensional(2D) mammography. Image quality and the radiation dose are of important concerns in breast CT imaging. The objective of this project is to investigate and develop innovative imaging configurations and reconstruction algorithms for obtaining accurate images and reducing radiation dose in breast CT imaging. During the second year of this project, I have continued the investigation of innovative imaging configuration and have implemented reconstruction algorithms considering different imaging configurations. I have also studied the application of total variation(TV)-based algorithm to sparse view reconstruction and have developed various methods to evaluate reconstruction-image quality. In summary, during the second year, I have successfully carried out research on the planned tasks, and the results obtained have formed a solid basis for me to continue the research planned for the next year.					
<b>15. SUBJECT TERMS</b> Breast CT, image reconstruction, scanning configuration, total variation minimization					
<b>16. SECURITY CLASSIFICATION OF:</b>			<b>17. LIMITATION OF ABSTRACT</b>  UU	<b>18. NUMBER OF PAGES</b>  45	<b>19a. NAME OF RESPONSIBLE PERSON</b> USAMRMC
<b>a. REPORT</b> U	<b>b. ABSTRACT</b> U	<b>c. THIS PAGE</b> U			<b>19b. TELEPHONE NUMBER (include area code)</b>

## Table of Contents

	<u>Page</u>
Introduction.....	4
Body.....	5
Key Research Accomplishments.....	10
Reportable Outcomes.....	11
Conclusion.....	13
References.....	14
Appendices.....	16

## INTRODUCTION

Breast cancer is the most frequently diagnosed cancer and the second leading cause of cancer mortality among women in the states [1]. Researchers are developing actively breast imaging techniques, including breast tomosynthesis [2] and dedicated breast computer tomography CT [3,4], which can form three-dimensional (3D) images of the breast, thus potentially overcoming inherent limitations of conventional two-dimensional (2D) mammography. Prototypes of dedicated breast CT scanners have been built in different institutions throughout the United States. Current scanners employ a circular imaging configuration for data collection and the FDK algorithm for approximate image reconstruction. However, it is well-known that a circular imaging configuration does not yield sufficient data for mathematically exact image reconstruction. Also, because the FDK algorithm requires data collected at a large number of projection views, and because the total dose in breast CT imaging is typically about the same as that in a two-view mammography, the number of photons collected at each view can be severely limited. As such, the projection data at each view have very low signal-to-noise ratio (SNR), thus severely limiting the breast-CT-image quality.

Clearly, image quality and radiation dose are great concerns in breast CT imaging. The objective of this research is to investigate and develop innovative imaging configurations and reconstruction algorithms for obtaining accurate images and reducing radiation dose in breast CT imaging. In the past year, my effort for the project have been supported by a Predoctoral Traineeship Award, and I have performed research tasks as planned. As discussed below, I have studied and assessed ROI imaging configurations for breast CT imaging by investigating data conditioning techniques and reconstructing images for the configurations. I have also conducted extensive studies using TV-based algorithms for a potentially substantial reduction of radiation dose in breast CT imaging. In addition to computer-simulation studies, I have performed real data studies involving physical phantoms and patient data provided by the collaborators. In summary, during the second year, I have successfully carried out research on the planned tasks, and the results obtained have formed a solid basis for me to continue the research planned for the next year.

## BODY

# 1 Research Accomplishments

## 1.1 Investigation of innovative imaging configurations

I have continued my effort in investigating the innovative imaging configurations for breast CT. In the second year, I have focused on the development and study of ROI imaging configuration for breast CT. I have performed a preliminary investigation on dynamic collimation to achieve targeted Region Of Interest (ROI) imaging using simulation studies [5], in which the source and the detector are moved for each view, so that after collimation, the ROI can always be covered by the beam. This imaging approach leads to an imaging problem with a relatively complex source trajectory and data truncation, which can however be solved with the back-projection filtration (BPF) algorithm [6,7]. Similar to a circular trajectory, this configuration can not provide data sufficient for exact image reconstruction for slice images that are not within the trajectory plane. In order to generate data sufficient for exact reconstruction of the 3D object, I studied a source trajectory, in which the object was translated along the rotation axis while the source and detector are moving around the object. This trajectory can generate data sufficient for exact image reconstruction of a 3D object. I used BPF algorithm to reconstruct ROI images from data acquired with this general trajectory. Both of these two studies employed a variable collimation approach to maximize dose efficiency. Variable collimation can be difficult to realize in real systems, I transformed variable collimation into a fixed collimation by taking the maximal collimation for all the views. This approach, however, may result unnecessary radiation to the region that is outside of the ROI. I am currently investigating ways to reduce the exposure to the region outside of the ROI for fixed collimation.

## 1.2 Investigation and development of novel algorithms for accurate reconstruction of breast CT images

**Implementation of reconstruction algorithms for different imaging configurations:** Continuing first year's effort, I have implemented the BPF algorithms for helical, saddle, and circle-plus-line imaging configurations. The implementation includes parameterization of the source trajectory, calculation of the derivative of the source trajectory and computation of backprojection and filtering. I generated simulation projection data using the Defrise disk phantom with different imaging configurations and then tested the algorithms using simulation data. I have also acquired real data with the prototype breast-CT scanner from a Defrise disk phantom. The system geometric information is obtained by a calibration procedure developed by our collaborators. The application of the reconstruction algorithm to real data requires projection data processing and source trajectory parameter fitting. I performed detector response correction and reference image conversion on the collected projection data first. From the recorded source locations, I then performed a least-square fitting to an ideal source trajectory. Using the fitting results, I parameterized the trajectory and calculated the source trajectory derivatives that are needed by BPF reconstruction algorithm. Results of the studies indicated that BPF reconstruction from a helical scanning configuration can provide images with less artifacts comparing to FDK reconstruction from a circular scanning configuration, especially for images not located within the trajectory plane. However, the volume coverage of a helical configuration is limited, and the chest wall can be difficult to cover. The saddle imaging configuration has a relative better volume coverage over the plane at  $z = 0$ . However, because of the mechanic limitation of the motor, the implementation of the saddle The

saddle trajectory is realized by small line segments connecting the precomputed points on the trajectory. It seems that the reconstruction algorithm is sensitive to this inaccuracy in the saddle configuration and serious artifact were generated in the reconstruction images from real data. I plan to further investigate the effects of this inaccuracy on the quality of the reconstruction image.

**Scatter compensation for real data:** In conventional screen-film mammography, anti-scatter grids are usually employed to reduce the degradation in image contrast due to X-ray scatter. However, in breast-CT imaging, the X-ray fluence incident on the detector at each view angle is much smaller than in conventional mammography due to dose considerations. Accordingly, it may not be advisable to employ anti-scatter grids in breast CT. For most of the existing reconstruction algorithms, it is assumed that projection data include only X-ray transmission on a straight line between the source and detector element. Inconsistencies introduced by scatter in data can lead to a decrease of low-contrast detectability, cupping artifacts, and streak artifacts between dense objects. Correction of scatter is a difficult problem because the precise form of the scattered radiation depends on the subject being scanned. Empirically, the scattered X-ray intensity does not have high-frequency component. Based on this, I developed empirical methods to estimate the scatter components. The first method is to use a cosine function that is relative flat across object to estimate the scatter component and this component is subtracted from the projection data. The magnitude of the cosine function is determined empirically by looking at the reconstruction image and verify if the cupping artifacts were removed. The second method is to use Monte Carlo simulation (SIERRA developed by Dr. John M. Boone) to estimate the scatter-to-primary ratio (SPR)[8]. Because the breast shape is close to a cylinder and its attenuation properties is close to water, I used water cylinders of different sizes in the Monte Carlo simulation. The SPRs of breast of other sizes were interpolated from the Monte Carlo simulation results.

**Noise studies of image reconstruction:** In breast-CT imaging, the total permissible radiation dose is in same order of that of a conventional mammographic examination. This can, however, result in data with a low signal-to-noise ratio (SNR) when projection data are acquired at a large number of views. So the noise propriety of the reconstruction algorithm can have an important effect on the reconstruction image. I have investigated how to improve the noise property of the reconstruction algorithm. my previous studies have shown that the original BPF algorithm involved a spatially varying weighting factor in the backprojection step. This weighting factor can not only increase the computation load, but also amplify the noise in reconstructed images. The weighting factor can be eliminated by appropriately rebinning the measured cone-beam data into fan-parallel-beam data. Such an appropriate data rebinning not only removes the weighting factor, but also retain other favorable properties of the BPF algorithm, ROI imaging reconstruction. To study the noise properties of the BPF algorithm and rebinned BPF algorithm for ROI imaging configuration, I have generated projection data of a uniform water cylinder phantom and added 1% of Gaussian noise. I then did 1000 noise realizations and reconstructed images with BPF and rebinned-BPF algorithms from these noisy data set. Using the 1000 images on the chords reconstructed from the noisy data sets, I calculated the empirical image variances on the chords. I also calculated the empirical image variances from the reconstructed images by use of the original BPF algorithm for comparison. The results show that the rebinned BPF algorithm can improve noise properties in terms of image variance.

### 1.3 Investigation and development of total-variation-based algorithms for breast CT image reconstruction

Radiation dose in breast-CT imaging is an important concern. Further dose reduction in breast CT can be achieved through collecting data at a reduced number of projection views. When analytic algorithms such as the FDK and BPF algorithms are applied to sparse-view data, the reconstruction images will contain artifacts such as streak artifacts that can lower significantly the image utility. Recently, algorithms based upon the minimization of image total variation (TV) subject to data condition have been developed for image reconstruction from sparse-view data [9,10,11]. I have performed a preliminary study in which TV-based algorithms have been exploited for image reconstruction from sparse-view patient data in breast CT in the first year. I have focused on studying the algorithm properties with real data during the second year.

**Studies of image quality of view number:** I performed an evaluation of the reconstruction algorithm with phantom data acquired with a bench-top CT system. The phantoms have both low-contrast spheres to simulate tumors and some small fine details. I did not scan it using the prototype breast CT because I want to perform a general-purpose study of the algorithm using the bench-top flat-panel CT system. A cylindrical phantom and an anthropomorphic head phantom was scanned and projection data of 960 views uniformly distributed over 0 to  $2\pi$  angular range was acquired. The cylindrical phantom is formed of SolidWater™ material (Gammex RMI, Madison WI), containing six different tissue-simulating plastic inserts with electron densities approximating cortical bone (2x), breast, brain, liver, and adipose tissues. There is a small high-contrast wire in the middle of the cylindrical phantom for resolution studies. The anthropomorphic head phantom was designed for realistically simulating human head [12], it features not only a natural human skeleton but also contrast-detail spheres approximating soft tissues. I then extracted 15, 30, 60, 96 and views of projection data from the 960-view data set and reconstructed images with both FDK and our TV-based reconstruction algorithms. Images reconstructed by use of FDK algorithm from the 960-view data set are used as the reference images. I performed three levels of image quality evaluation on the reconstruction image: qualitative-visualization-based evaluation, quantitative-metric-based evaluation and task-specific evaluation. The evaluation results demonstrate that, for the experimental imaging conditions under consideration, the TV-based algorithm consistently reconstructs images of quality comparable to that of the FDK-reference image from data that are much less than the full data currently used. These results demonstrate the potential for TV-based reconstruction algorithms to yield high image quality at significantly reduced view sampling.

**Studies of effects of reconstruction parameters on quality of reconstructed images:** Breast imaging requires both high contrast and spatial resolution because both low-contrast tumors and calcifications are of interests to doctors. Because of the high noise level in breast CT data, the reconstruction from breast CT data is more challenging. Special considerations need to be paid in selection of the parameters of the reconstruction problem. The selection of the system matrix plays a very important role for such an inconsistent system. The system matrix is determined by the number of measurements, image array size, and the projection model. After measurements are given, choices of different image array sizes and projection models will also change the linear system, and it is possible to improve the image reconstruction quality of breast CT images by choosing appropriate image array size and projection model. High spatial resolution requires a smaller pixel size and thus a larger image array. However, for TV-based algorithms, a larger image array size increases the number of unknowns and make the linear system more under-determined, which in turn requires more measurements. Therefore, when choosing an image

array size, the number of measurements needs to be carefully taken into consideration. I have studied the effect of image array size on reconstruction-image quality using full 500-view projections of patient data sets. When the image sampling density is greater than the sampling density of projection data, the effect of further increase of image array size on reconstruction images by use of FDK algorithm is linear. For TV-based algorithms, the effect is non-linear because of the change of image array size changes the system matrix. The increase of image array size will increase the underdetermineness of the linear system. I have increased the image sampling density up to four times of detector sampling density. Overall, the TV reconstruction images are similar to FDK reconstruction with hanning filter. It seems that TV-based algorithm can generate calcifications of higher contrast comparing with FDK algorithms when the background noise level is similar. As part of my algorithm evaluation studies, I also studied the effect of reconstruction parameters on the reconstruction image quality. There is one key parameter for the TV-based reconstruction problem which controls the impact level of data inconsistency. I varied this parameter for different sparse data sets and studied the impacts of this parameter. In general, this parameter must be larger than 0 in order for there to be a feasible image because of inconsistency between actual data and system model. Relaxing this parameter (going to larger values), will yield images with lower TV, thereby allowing for greater TV regularization. If this parameter is too large, blocky and cartoonish images can be generated.

## 1.4 Evaluation of the proposed configurations and algorithms

**Generation of simulation data:** I have created and modified a digital breast phantom that consists of a half-ellipsoid object wrapped by a simulated skin containing a compound of adipose and glandular tissue, which are also approximated by ellipsoids of different sizes. Spheres with strong attenuation (i.e., high contrast) of different sizes that mimic micro-calcifications (MCCs) have also been included in the phantoms. In a typical MCC, the smallest calcification is about 200  $\mu\text{m}$ , and a MCC typically includes 3 to 10 simulated micro-calcifications. The MCCs have been added to the glandular tissues and the axillary tail of the breast. I have generated projection data in different ways with the simulation phantom using the same geometry and configuration as the prototype system: 1. Data were generated from a discrete image of the objects and discrete projections were calculated from the discrete images. These are referred to as discrete projection data. For iterative reconstruction, the imaging process is modeled by a discrete linear system. One can choose a system matrix that is exactly the same as what is used to generate the projection data. There is no model inconsistency for this situation, and the image is expected to be completely recovered when there are enough measurements. Using this property, discrete projections were used to verify if the iterative algorithms are correctly implemented. I used this as a preliminary test of the algorithm. 2. Projection data were also calculated from analytic objects, which are referred to as analytic projection data. One cannot find a system matrix that can exactly represent the continuous projection model for analytic projection data. No matter how the system matrix is chosen for the linear system, there will always be an inconsistency between the estimated projection data and the measured projection data. This type of inconsistency is referred to as continue-to-discrete inconsistency, which makes reconstruction from analytic projection data more challenging than the discrete projection data for optimization-based algorithms. I have used analytic projection data for general algorithm evaluation. 3. I have also added Gaussian noise to the projection data. Adding noise to the projection data makes the data more realistic and can serve as a further validation for the reconstruction algorithms. Gaussian noise model is generally a good approximation for the data noise in CT. I have added different levels of Gaussian



noise to the projection data to simulate noises in real data, from which I then performed image reconstruction studies.

**Design of a physical breast phantom:** I have also designed a physical breast phantom using available commercial plastic materials. The physical breast phantom is similar to the digital breast phantom. I used small wires of different sizes to simulate MCCs. Considering the detector pixel size of 0.388 mm, I used wires of diameters from 0.3 mm to 0.8 mm. I used polystyrene as the background materials since its attenuation properties is similar to water. I then looked into a number of plastics materials that have similar attenuation properties as adipose tissue, breast cancer, and glandular tissue. Based on the attenuation properties and commercial availability, I have chosen five different materials with CT numbers ranging from -100 to +120, including LDPE, HDPE, polycarbonate, and acrylics. I then placed these low-contrast objects into mid-plane and off-mid-plane of the phantom. The contrast levels of some of the low-contrast objects chosen are lower than the adipose and glandular tissues so that I can have an idea on the limit of the current imaging configuration and reconstruction algorithms. I plan to scan this phantom with a diagnostic scanner first and calibrate the CT number of the different materials since the current X-ray spectrum of the prototype breast CT scan is close to the spectrum of diagnostic scanner at 80 kVp. I then will scan this phantom with the prototype breast CT scanner and calculate the detectability of the low contrast objects.

**Evaluation of reconstruction image quality:** I have developed three-level evaluation methods for images reconstructed from real data collected with an bench-top scanner. 1. I first conducted a qualitative evaluation by visual inspection and comparison of reconstructed images. To reveal the structure and contrast details in a reconstruction, I displayed selected regions of interest (ROIs) with a narrowed display grayscale and/or zoomed-in views. Although visual inspection of images provides only a qualitative comparison of algorithm performance, it can be an informative assessment of the image quality, especially in the presence of image artifacts that are otherwise difficult to quantify meaningfully by use of general metrics. When a narrow grayscale window is used, it may reveal considerable reconstruction artifacts that may be otherwise invisible in a wide grayscale window. 2. I also used a number of technical-efficacy-based metrics, including contrast-to-noise ratio (CNR), universal quality index (UQI) [13], Pearson correlation coefficient (PCC), and mutual information (MI) [14], which are explained in details in the appendix [15]. The CNR evaluates the signal to noise ratio of the reconstructed image, while PCC, UQI and MI evaluate the similarity between reconstructed images and the reference image. Each metric only evaluates a certain aspect of the reconstruction quality and is not necessary a direct indication of the utility of the images. 3. I also performed task-specific evaluation. In breast imaging, people are generally interested in the detectability of a calcification or tumor. The former is usually a small high-contrast object and the latter is a low-contrast object. The evaluation study used a model observer for a detection task. This model observer is similar to the widely used pre-whitening observer. Although the analysis here from measured data does not strictly obey the rigorous assumptions of linearity, shift invariance, and other conditions [16,17], detectability provides a quantitative metric of relative comparison in task performance among the various sparse-view reconstructions [18,19]. The “signal”, which is the high-contrast wire in the cylindrical phantom and the low-contrast, extended tumor in the head phantom, have be extracted and signal masks was applied to the reconstructed images. The background image will be estimated from a region surrounding the signal region. From the obtained signal image, I have subsequently computed the image-energy spectrum and then obtain the detectability indices for reconstructed images. Please refer to appendix for details.

## KEY RESEARCH ACCOMPLISHMENTS

- I have investigated variable and fixed collimation for ROI imaging on breast CT.
- I have investigated and implemented BPF reconstruction algorithms for helical, saddle, and circle-plus-line imaging configurations for potential use in breast CT.
- I have investigated and implemented BPF reconstruction algorithms for ROI imaging configurations for potential use in breast CT.
- I have performed scatter correction using empirical methods on real patient data acquired with breast CT.
- I have performed noise study for the BPF and rebinned-BPF algorithms.
- I have studied the image quality change versus number of views for TV-based reconstruction algorithm with real data.
- I have studied effects of reconstruction parameters on the quality of reconstructed images.
- I have refined the simulation data generation with the digital breast phantom.
- I have designed a physical breast phantom for real data experiment.
- I have developed a set of evaluation methods for evaluation of reconstruction image quality.

## REPORTABLE OUTCOMES

### Peer-reviewed Journal Papers

1. **J. Bian**, J. H. Siewerdsen, X. Han, E. Y. Sidky, J. L. Prince, C. A. Pelizzari, and X. Pan, "Evaluation of sparse-view reconstruction from flat-panel-detector cone-beam CT," *Physics in Medicine and Biology*, Vol. 55, pp 6575-6599, 2010. **(Featured article of *Physics in Medicine and Biology*, published online on Oct-20, 2010, one of the ten most read articles of the journal a few days after its publication until now (Feb-2011), was selected as part of the journal's highlights collection of 2010, cover story of Medicalphysicsweb Review of winter 2011, one of the ten candidates of Roberts' Prize for best paper in *Physics in Medicine and Biology* and the results will be announced in September, 2011. )**
2. X. Han, **J. Bian**, D. R. Eaker, T. L. Kline, E. Y. Sidky, E. L. Ritman, and X. Pan, "Algorithm-enabled low-dose micro-CT imaging," *IEEE Transactions on Medical Imaging*, 2010 (in press).
3. D. Xia, X. Xiao, **J. Bian**, X. Han, E. Y. Sidky, F. De Carlo, and X. Pan, "Image Reconstruction from sparse data in synchrotron-radiation-based micro-tomography," *Review of Scientific Instruments* (accepted).

### Conference Proceeding Articles

1. **J. Bian**, J. Wang, X. Han, E. Y. Sidky, J. Ye. L. Shao, and X. Pan, "Reconstruction from sparse data in offset-detector CBCT," *Proceeding of the First International Meeting on Image Formation in X-Ray Computed Tomography*, pp 96-100, 2010.
2. D. Xia, **J. Bian**, X. Han, E. Y. Sidky, J. Lu, O. Zhou, and X. Pan, "Investigation of image reconstruction in CT with a limited number of stationary sources," *Proceeding of the First International Meeting on Image Formation in X-Ray Computed Tomography*, pp 90-95, 2010.
3. X. Xiao, D. Xia, **J. Bian**, X. Han, E. Y. Sidky, F. D. Carlo, and X. Pan, "Image reconstruction from highly sparse data of fast synchrotron-based micro-tomography of biomedical samples," *Proceeding of the First International Meeting on Image Formation in X-Ray Computed Tomography*, pp 156-161, 2010.
4. **J. Bian**, X. Han, J. Wang, E. Y. Sidky, L. Shao, and X. Pan, "Low-dose CT in SPECT/CT patient scan," *Proceedings of IEEE Nuclear Science Symposium and Medical Imaging Conference*, M04-5, 2010.
5. **J. Bian**, X. Han, E. Y. Sidky, J. H. Siewerdsen, and X. Pan, "Investigation of low-contrast tumor detection in algorithm-enabled low-dose CBCT," *Proceedings of IEEE Nuclear Science Symposium and Medical Imaging Conference*, M19-235, 2010.

### Conference Presentations and Abstracts

1. **J. Bian**, J. Wang, X. Han, E. Y. Sidky, J. Ye. L. Shao, and X. Pan, "Reconstruction from sparse data in offset-detector CBCT," *The First International Meeting on Image Formation in X-Ray Computed Tomography*, Salt Lake City, UT, 2010.
2. D. Xia, **J. Bian**, X. Han, E. Y. Sidky, J. Lu, O. Zhou, and X. Pan, "Investigation of image reconstruction in CT with a limited number of stationary sources," *The First International Meeting on Image Formation in X-Ray Computed Tomography*, Salt Lake City, UT, 2010.

3. X. Xiao, D. Xia, **J. Bian**, X. Han, E. Y. Sidky, F. D. Carlo, and X. Pan, "Image reconstruction from highly sparse data of fast synchrotron-based micro-tomography of biomedical samples," *The First International Meeting on Image Formation in X-Ray Computed Tomography*, Salt Lake City, UT, 2010.
4. X. Xiao, D. Xia, **J. Bian**, X. Han, E.Y. Sidky, F. De Carlo, and X. Pan, "Image reconstruction from highly sparse data in fast synchrotron-based imaging," *SPIE Optical Engineering*, San Diego, CA, 2010
5. **J. Bian**, X. Han, J. Wang, E. Y. Sidky, L. Shao, and X. Pan, "Preliminary experience in sparse-view reconstruction from clinical patient data in offset-detector CBCT," *IEEE Nuclear Science Symposium and Medical Imaging Conference*, M04-5, Knoxville, TN, 2010.
6. **J. Bian**, X. Han, E. Y. Sidky, J. H. Siewerdsen, and X. Pan, "Investigation of low-contrast tumor detection in algorithm-enabled low-dose CBCT," *IEEE Nuclear Science Symposium and Medical Imaging Conference*, M19-235, Knoxville, TN, 2010.
7. X. Han, **J. Bian**, E.Y. Sidky, and X. Pan, "Feasibility study of low-dose intra-operative cone-beam CT for image-guided surgery," *SPIE Medical Imaging*, Orlando, FL, 2011

## CONCLUSIONS

During the second year of the project, I have investigated and evaluated ROI imaging configurations potentially useful for breast CT imaging by performing simulation studies. I have developed and modified BPF algorithms to reconstruct images within an ROI from data containing truncations for different imaging configurations. In an attempt to further reduce imaging dose, one may reduce the number of views at which projection data are collected. In this situation, analytic algorithms may not provide adequate results. Instead, I have developed, modified, and implemented the TV-based algorithm to reconstruct images from sparse-view data and evaluated the algorithm using real data. I have also refined projection data generation from digital breast phantoms that can be used as an important tool for evaluation of the potential utility of imaging configurations and reconstruction algorithms. I also designed a physical breast phantom that can be used in real data experiment. Furthermore, I have developed a set of evaluation methods and have performed evaluation studies of images reconstructed from real data.

In summary, I have achieved the goals planned for the second year and laid down the foundation for the research in the next year. The aims in the next year include further development of the TV-based algorithm for image reconstruction in low-dose breast CT, investigation of the effects of exposure on the quality of image reconstruction with real breast phantom data.

## REFERENCES

1. Cancer Fact and Figures, American Cancer Society, 2010, (<http://www.cancer.org/research/cancerfactsfigures/cancerfactsfigures/cancer-facts-and-figures-2010>)
2. J. T. Dobbins III and D. J. Godfrey, "Digital X-ray tomosynthesis:current state of the TV and clinical potential", *Phys. Med. Biol.*, Vol. 48, pp. R65–R106, 2003. A
3. J. M. Boone, A. L. Kwan, K. Yang, G. W. Burkett, K. K. Lindfors and T. R. Nelson, "Computed tomography for imaging the breast", *J. Mammary Gland Biol. Neoplasia*, Vol.11, pp. 103–111, 2006.
4. Chen B and Ning R, "Cone-beam volume CT breast imaging: Feasibility study", *Med. Phys.*, Vol 29, pp. 755–770, 2002.
5. J. Bian, H. Zhang, P. Zhang, and X. Pan, "A cone-beam Approach of ROI Imaging with a Detector Smaller than the Imaged Object", *Proceeding of 9th International Meeting on Fully Three-Dimensional Image Reconstruction in Radiology and Nuclear Medicine*, pp. 386–389, 2007
6. Y. Zou, and X. Pan, "Exact image reconstruction on PI-line from minimum data in helical cone-beam CT", *Phys. Med. Biol.*, Vol 49, pp. 941–959, 2004.
7. Y. Zou, and X. Pan, and E. Y. Sidky, "Theory and algorithms for image reconstruction on chords and within regions of interest", *J. Opt. Soc. Am. A*, Vol 22, pp. 2372–2384, 2005.
8. J. M. Boone, M. H. Buonocore, and V. N. Cooper III, "Monte carlo validation in diagnostic radiological imaging," *Med. Phys.*, vol. 27, pp.1294–1304, 2000.
9. E. Y. Sidky, C.-M. Kao, and X. Pan, "Accurate image reconstruction from few-views and limited-angle data in divergent-beam CT", *J. X-ray Sci. Tech.*, Vol. 14, pp. 119–139, 2006.
10. E. Y. Sidky and X. Pan, "Image reconstruction in circular cone-beam computed tomography by constrained, total-variation minimization", *Phys. Med. and Bio.*, Vol. 53, pp. 4777–4807, 2008.
11. X. Pan, E. Y. Sidky, and M. Vannier, "hy do commercial CT scanners still employ traditional, filtered back-projection for image reconstruction?" *Inverse Probl.*, vol. 25, p. 123009, 2009.
12. C. B. Chiarot, J. H. Siewerdsen, T. Haycocks, D. J. Moseley, and D. A. Jaffray, "An innovative phantom for quantitative and qualitative investigation of advanced X-ray imaging technologies," *Phys. Med. Biol.*, Vol. 50, pp. N287–N297, 2005.
13. Z. Wang and A. Bovik, "A universal image quality index," *IEEE Signal Process. Lett.*, Vol. 9, pp. 81–84, 2002.
14. J. P.W. Pluim, J. B. A. Maintz, and M. A. Viergever, "Mutual-informationbased registration of medical images: a survey," *IEEE Trans. Med. Imag.*, Vol. 22, pp. 986–1004, 2003.
15. J. Bian, J. H. Siewerdsen, X. Han, E. Y. Sidky, J. L. Prince, C. A. Pelizzari, and X. Pan, "Evaluation of sparse-view reconstruction from flat-paneldetector cone-beam CT," *Phys. Med. Biol.*, vol. 55, pp. 6575–6599, 2010.

16. International Commission on Radiation Units and Measurements, "Medical image—the assessment of image quality," Bethesda, MD, Tech. Rep. ICRU Report No. 54, 1996.
17. A. E. Burgess, F. L. Jacobson, and P. F. Judy, "Human observer detection experiments with mammograms and power-law noise," *Med. Phys.*, Vol. 28, pp. 419–437, 2001.
18. J. H. Siewerdsen and D. A. Jaffray, "Optimization of X-ray imaging geometry (with specific application to flat-panel cone-beam computed tomography)," *Med. Phys.*, Vol. 27, pp. 1903–1914, 2000.
19. I. S. Reiser and R. M. Nishikawa, "Task-based assessment of breast tomosynthesis: Effect of acquisition parameters and quantum noise," *Med. Phys.*, vol. 37, pp. 1591–1600, 2010.

## APPENDICES

- Appendix A: **J. Bian**, J. H. Siewerdsen, X. Han, E. Y. Sidky, J. L. Prince, C. A. Pelizzari, and X. Pan, "Evaluation of sparse-view reconstruction from flat-panel detector cone-beam CT," *Phys. Med. Biol.*, vol. 55, pp. 6575–6599, 2010. **(Featured article of *Physics in Medicine and Biology*, published online on Oct-20, 2010, one of the ten most read articles of the journal a few days after its publication until now (Feb-2011), was selected as part of the journal's highlights collection of 2010, cover story of Medicalphysicsweb Review of winter 2011, one of the ten candidates of Roberts' Prize for best paper in *Physics in Medicine and Biology* and the results will be announced in September, 2011. )**
- Appendix B: **J. Bian**, X. Han, E. Y. Sidky, J. H. Siewerdsen, and X. Pan, "Investigation of low-contrast tumor detection in algorithm-enabled low-dose CBCT," *Proceedings of IEEE Nuclear Science Symposium and Medical Imaging Conference*, M19-235, 2010.



# Evaluation of sparse-view reconstruction from flat-panel-detector cone-beam CT

Junguo Bian<sup>1</sup>, Jeffrey H Siewerdsen<sup>3</sup>, Xiao Han<sup>1</sup>, Emil Y Sidky<sup>1</sup>,  
Jerry L Prince<sup>4</sup>, Charles A Pelizzari<sup>2</sup> and Xiaochuan Pan<sup>1,2</sup>

<sup>1</sup> Department of Radiology, The University of Chicago, Chicago, IL, USA

<sup>2</sup> Department of Radiation & Cellular Oncology, The University of Chicago, Chicago, IL, USA

<sup>3</sup> Departments of Biomedical Engineering, Johns Hopkins University, Baltimore, MD, USA

<sup>4</sup> Department of Electrical & Computer Engineering, Johns Hopkins University, Baltimore, MD, USA

Received 9 July 2010, in final form 13 August 2010

Published 20 October 2010

Online at [stacks.iop.org/PMB/55/6575](http://stacks.iop.org/PMB/55/6575)

## Abstract

Flat-panel-detector x-ray cone-beam computed tomography (CBCT) is used in a rapidly increasing host of imaging applications, including image-guided surgery and radiotherapy. The purpose of the work is to investigate and evaluate image reconstruction from data collected at projection views significantly fewer than what is used in current CBCT imaging. Specifically, we carried out imaging experiments using a bench-top CBCT system that was designed to mimic imaging conditions in image-guided surgery and radiotherapy; we applied an image reconstruction algorithm based on constrained total-variation (TV)-minimization to data acquired with sparsely sampled view-angles and conducted extensive evaluation of algorithm performance. Results of the evaluation studies demonstrate that, depending upon scanning conditions and imaging tasks, algorithms based on constrained TV-minimization can reconstruct images of potential utility from a small fraction of the data used in typical, current CBCT applications. A practical implication of the study is that the optimization of algorithm design and implementation can be exploited for considerably reducing imaging effort and radiation dose in CBCT.

(Some figures in this article are in colour only in the electronic version)

## 1. Introduction

Flat-panel-detector x-ray cone-beam computed tomography (CBCT) is used in a rapidly increasing host of imaging applications. Although current flat-panel-detector CBCT (for convenience, we simply refer to flat-panel-detector CBCT as CBCT throughout the paper) is not designed generally for achieving image quality of advanced diagnostic CT in terms of spatial, contrast and temporal resolution, it can yield images containing information of

high practical utility in image-guided interventions and have a greater scanning-configuration flexibility than diagnostic CT. C-arm CBCT in surgery and on-board CBCT in radiotherapy represent two examples of medical CBCT applications for determining the position and status of a target area and the surrounding tissues inside a patient.

As in diagnostic CT, radiation dose to the subject in CBCT imaging is also a paramount concern. In particular, when CBCT is used for guiding and evaluating interventional procedures, repeated scans of the same subject are carried out, such as multiple scans during a surgical operation or over the course of fractionated radiation therapy. Therefore, the accumulated radiation dose of repeated CBCT imaging to the patient poses a serious radiation safety concern. Studies indicate that dose from CT scans may have a lifetime attributable risk of cancer higher than previously assumed (Brenner and Hall 2007, Gonzalez *et al* 2009, Smith-Bindman *et al* 2009). Reducing CT dose has been an area of active research in medical imaging. In CBCT, one can reduce imaging dose by reducing the number of projection views at which data are collected. The use of fewer projection views can also lead to a reduced imaging time in step-and-shoot CBCT, improving workflow and minimizing potential motion artifacts. However, reducing the number of projection views leads to a challenging image-reconstruction task. When the projection views are sparsely sampled, the analytic reconstruction algorithms (Feldkamp *et al* 1984, Katsevich 2002, Zou and Pan 2004, Pack *et al* 2005), which require densely sampled projection views, can result in prominent streak artifacts (Brooks *et al* 1979, Crawford and Kak 1979). Efforts have been made to interpolate additional projection views from measured data (La Riviere and Pan 1999, Galigekere *et al* 1999). Such an approach may be useful for certain scanning configurations and particular subjects. It is, however, difficult to make general conclusions about the practical utility of such an approach. Prior efforts exist in developing algorithms for image reconstruction from parallel- and fan-beam projections (Delaney *et al* 1998, Loose and Leszczynski 2001) or cone-beam projections of sparse objects (Li *et al* 2002) acquired at a small number of views, some of which can be extended to image reconstruction from CBCT data acquired at a reduced number of views.

Initial papers (Candès *et al* 2006a, Candès *et al* 2006b), which led off the study of compressive sensing (CS) as a distinct field, showed examples of image reconstruction from ideal, sparse Fourier data using constrained minimization of the image's total variation (TV). The illustrated Fourier sampling patterns, and results, were highly suggestive and encouraging for sparse-view sampling in CT. Recent work on translating constrained TV-minimization to application with divergent-beam transforms indeed showed, largely in simulation, that highly accurate image reconstruction from sparsely sampled projection views may be possible (Sidky *et al* 2006). An adaptive steepest descent-projection onto convex sets (ASD-POCS) algorithm, for accurately solving constrained TV-minimization with the divergent-beam transform was formalized (Sidky *et al* 2006, Sidky and Pan 2008); the ASD-POCS algorithm combines steepest descent on the image TV with an adaptive step size and POCS to enforce image constraints, including a tolerance on the data divergence.

Under ideal conditions of noiseless simulation, it appears that sparse-view sampling in CT can yield exact reconstruction. But theoretically there is, as yet, no proof of an exact recovery principle (ERP) (Candès *et al* 2006a) for the divergent-beam transform. Our limited study on the 2D Radon transform (Sidky *et al* 2010) using the restricted isometry principle (RIP) (Candès and Wakin 2008) yields very large isometry constants, which would seem to exclude an ERP. Yet, these sampling configurations appear to yield highly accurate reconstruction in simulation even with challenging phantoms designed to 'break' the algorithm. This apparent contradiction, however, is likely due to the fact that CS theory for deterministic sampling is not yet mature enough to be applied to the x-ray transform. The aim of this work is to carry out a comprehensive study of the use of constrained TV-minimization for sparse-view reconstruction

of real CT data, which contain various non-idealities with respect to the ideal imaging model. In the study, data were collected in two imaging experiments using a bench-top CBCT system that was designed to mimic imaging conditions in image-guided surgery and radiotherapy. We show that the ASD-POCS algorithm for solving constrained TV-minimization is effective at mitigating artifacts that often dominate sparse-view image reconstruction.

A major question, hardly addressed in the literature, is that, even though algorithms based on constrained TV-minimization appear to effectively remove streaks, other aspects of image quality have never been carefully analyzed. Indeed, application of TV regularization is criticized often for producing blocky, cartoonish images. To address this concern, we display a multitude of images showing various ROIs at different contrast levels. In addition to this, we employ a spectrum of quantitative performance metrics from the image science literature with the purpose of rigorously elucidating image quality characteristics of resulting reconstructions, including image noise, correlation, similarity (to a ‘true’ reference image) and task-based detectability. In particular, some metrics can be impacted by subjective qualities such as blockiness. To gauge the performance of the ASD-POCS algorithm, we also included reconstruction and evaluation results obtained with carefully coded implementations of the expectation-maximization (EM) (Dempster *et al* 1977, Shepp and Vardi 1982) and projection-onto-convex-sets (POCS) (Gordon *et al* 1970, Youla and Webb 1982, Combettes 1993) algorithms.

The paper is organized as follows. In section 2, we discuss the bench-top CBCT system, data acquisition and imaged subjects. In section 3, reconstruction algorithms, including the EM, POCS and ASD-POCS algorithms, are described. A leading focus of the work is to carry out an extensive, quantitative evaluation of image quality. Therefore, we introduce in section 4 a number of evaluation metrics that are designed for characterizing different aspects of multi-faceted image quality. In sections 5–7, we present and analyze in detail the study results, which are followed by discussion and conclusion in sections 8 and 9, respectively.

## 2. CBCT system and data acquisition

### 2.1. CBCT system

A bench-top CBCT system (Tward and Siewerdsen 2008), developed to simulate imaging tasks in image-guided surgery and radiotherapy, was used in this study. The x-ray tube has a 0.4–0.8 mm focal spot and 14° anode (Rad94 in Sapphire, Varian Medical Systems, Salt Lake City, UT) powered by a constant potential generator CPX-380 (EMD Inc., Montreal, QC); the flat-panel detector, with a pitch of 400  $\mu\text{m}$ , was based on a  $1024 \times 1024$  ( $41 \times 41 \text{ cm}^2$ ) active matrix of a-Si:H photo diodes, thin-film transistors and CsI:Tl x-ray converter (RID-1640A, PerkinElmer Optoelectronics, Santa Clara, CA), and the imaged subject was placed on a rotation stage. The distances of the source to the center of rotation and to the detector plane were 93.5 cm and 144.4 cm, respectively, yielding a field of view (FOV) of  $26 \times 26 \times 26 \text{ cm}^3$ . In our experiments, to mimic typical imaging conditions in image-guided surgery and radiotherapy, we used a circular trajectory to collect data at 120 kVp exposure. In the imaging coordinate system, the trajectory is within a plane at  $z = 0 \text{ cm}$ . We also added a filtration of 2.0 mm Al + 1.1 mm Cu to the source so that it yields beam quality comparable to that of clinical CT scanners. An anti-scatter grid was not used in the current study. The mAs per projection was 1.2 mAs. The dose (to the center of a 16 cm water cylinder) therefore varied linearly from 0.39 mGy at 30 views to 12.43 mGy at 960 views, resulting an effective dose of about 0.023 mSv and 0.74 mSv to the head for 30 and 960 views, respectively.

## 2.2. Experimental phantoms

We used two phantoms: a cylindrical phantom and an anthropomorphic head phantom. Images displayed in row 1 of figure 1 were reconstructed from full, 960-view data using the FDK algorithm. Because the ‘truth’ of the physical phantoms is unknown, we use the images as the surrogate ‘truth’ and refer to them as the FDK-reference images. The cylindrical phantom is formed of 16 cm diameter SolidWater<sup>TM</sup> material (Gammex RMI, Madison, WI), containing six different tissue-simulating plastic inserts with electron densities approximating cortical bone (2×), breast, brain, liver and adipose tissue. In addition, the central region of the cylindrical phantom also has an air pencil-chamber cavity with an inserted thin wire. Although the spatial structure of the cylindrical phantom is relatively simple, different contrast levels offered by different inserts provide an opportunity to evaluate reconstruction contrast and spatial resolution. The anthropomorphic head phantom was designed for realistically simulating a human head (Chiarot *et al* 2005). It features not only a natural human skeleton but also contrast-detail spheres approximating soft tissues. These fine and low-contrast structures pose challenges for tasks of image reconstruction from reduced numbers of projections and provide opportunities for evaluating algorithm performance.

## 2.3. Data acquisition

In the experiment, data were collected from each of the two phantoms with the detector at a rate of about 1 frame per second. We estimated reference measurements (i.e.  $I_0$ ) by averaging the detector-pixel values over a selected region on the detector plane corresponding to the unattenuated beam. Subsequently, projection data were calculated from the reference and transmission measurements. In each of the two imaging experiments, we collected measurements at 960 views uniformly distributed over  $2\pi$  and converted them into projection data. Throughout the paper, we refer to the 960-view data as the *full* data. Images displayed in figure 1 were reconstructed from the full data sets of the phantoms using the FDK and ASD-POCS algorithms, which, as mentioned above, were used as the surrogate truth for the corresponding phantoms and are referred to as *FDK-reference* and *ASD-POCS-reference* images. In the study below, we extracted sparse-view data from the full data.

## 3. Reconstruction algorithms

### 3.1. Imaging model

In practical imaging applications, data  $\mathbf{g}$  acquired, and image  $\mathbf{f}$  reconstructed, can be interpreted as vectors of sizes  $M$  and  $N$ , i.e.  $\mathbf{g} = (g_1, g_2, \dots, g_M)^T$  and  $\mathbf{f} = (f_1, f_2, \dots, f_N)^T$ , where  $T$  denotes the matrix transpose, and  $M$  and  $N$  the numbers of transmission rays and image voxels, respectively. We assume that the imaging model in CBCT is a discrete linear system:

$$\mathbf{g} = \mathcal{H}\mathbf{f}, \quad (1)$$

where  $\mathcal{H}$  is an  $M \times N$  system matrix modeling the cone-beam x-ray transform. With this discrete data model, image reconstruction can be thought of as an inversion of equation (1) given the knowledge of the projection data. In practical CBCT imaging, the huge size of the linear system prevents one from directly inverting equation (1). Moreover, for problems such as image reconstruction from a reduced number of projections, the linear system can be severely under-determined, i.e.  $M \ll N$ , admitting multiple solutions. Obviously, a particular entry of  $M$  depends on the selection of image-expansion basis set and the discrete computation of the

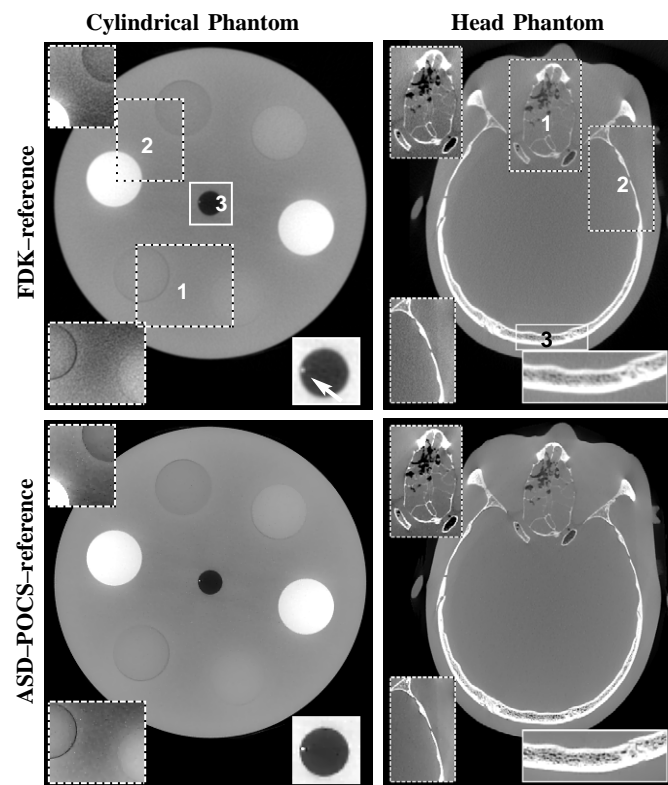


**Figure 1.** Images of the cylindrical and head phantoms within a transverse slice at  $z = 0$  cm reconstructed from full data using the FDK (row 1) and ASD-POCS (row 2) algorithms. For the cylindrical phantom, the entire images are displayed with a wide (i.e. bone-grayscale) window  $[-1000, 714]$  HU; rectangle regions enclosed by dashed lines (i.e. ROIs 1 and 2) are re-displayed in the upper-left and lower-left corners with a narrow (i.e. soft-tissue-grayscale) window  $[-257, 143]$  HU, and the rectangle region enclosed by solid lines (i.e. ROI 3) is re-displayed in the lower-right corner with a zoomed-in view in a grayscale window of  $[-1000, -143]$  HU, with an arrow pointing to a wire insert. For the head phantom, the entire images are displayed with a wide bone-grayscale window  $[-1000, 1000]$  HU; ROIs 1 and 2 are re-displayed in the upper-left and lower-left corners with a narrow window  $[-429, 429]$  HU and ROI 3 is re-displayed in the lower-right corner using a zoomed-in view with the bone-grayscale window.

x-ray transform. Throughout the work, we have used voxels as the image-expansion-basis set and a ray-driven projector for computing the x-ray transform.

### 3.2. EM and POCS algorithms for unconstrained optimization reconstruction

An optimization-based approach can be designed for reconstructing images, which generally consists of an optimization formulation and algorithms solving for the formulation. For the CBCT-imaging model in equation (1), an unconstrained minimization problem can be devised in which the objective function is the Kullback-Leibler (KL) divergence between the measured and estimated data (Barrett and Myers 2003). It is well-known that the EM algorithm yields a solution to the unconstrained minimization problem through minimizing the KL-data divergence. In this work, for comparison, we implemented the EM algorithm

and compared its reconstruction with those of other algorithms. Because the POCS algorithm is used widely for solving a discrete linear system in equation (1) and because, as shown below, it is used as a component of the ASD-POCS algorithm, we also implemented the POCS algorithm and compared its reconstruction with those of other algorithms under study. In fact, when data are consistent with the imaging model in equation (1), the POCS algorithm solves an unconstrained minimization problem in which the object function is the Euclidean-data divergence:

$$D(\mathbf{f}) = |\mathcal{H}\mathbf{f} - \mathbf{g}|. \quad (2)$$

In the numerical studies described below, the POCS and EM algorithms were terminated at 240 and 300 iterations, which were chosen at which the Euclidean- and KL-data divergences change little for the cases under study. Throughout the study,  $\mathbf{f} = \mathbf{0}$  and  $\mathbf{1}$  were used as the initial image estimates for POCS and EM algorithms, respectively.

### 3.3. ASD-POCS algorithm for constrained TV-minimization reconstruction

The POCS and EM algorithms provide solutions to unconstrained optimization problems in which the Euclidean- and KL-data divergences, respectively, are the objective functions. For under-sampled data, where  $M \ll N$  the solution arrived at by these algorithms can generally be dependent on initial images. As discussed in detail previously (Sidky *et al* 2006, Sidky and Pan 2008, Pan *et al* 2009), image reconstruction based upon equation (1) can also be formulated as a constrained optimization problem:

$$\mathbf{f}^* = \operatorname{argmin} \|\mathbf{f}\|_{\text{TV}} \quad \text{s.t.} \quad D(\mathbf{f}) \leq \epsilon \quad \text{and} \quad f_n \geq 0, \quad (3)$$

where  $\|\mathbf{f}\|_{\text{TV}}$ , referred to as the image TV, denotes the  $\ell_1$  norm of the discrete gradient magnitude of the image. This optimization formulation selects the image with minimum TV amongst those that satisfy the constraints, and the solution can be unique even when  $M \ll N$ . The data divergence  $D$  can reach zero in the absence of data inconsistency. In practice, however, measurements always contain inconsistent components, and a tolerance parameter  $\epsilon$  (discussed further below) is selected for controlling the impact level of potential data inconsistency on image reconstruction (Sidky and Pan 2008).

We point out here that there is a distinction between an iterative reconstruction algorithm and the optimization formulation upon which an algorithm is based. For example, the iteration of the EM algorithm is often truncated well short of convergence to the minimizer of the KL-data divergence. One of the themes of this work is to investigate the properties of the solution to equation (3). To attain this, we employed the same ASD-POCS algorithm as that described in detail in Sidky and Pan (2008) to accurately solve the constrained TV-minimization problem in equation (3). An efficient form of ASD-POCS was developed for application to digital breast tomosynthesis (Sidky *et al* 2009). But the algorithm was designed to yield clinically useful images in less than 20 iterations, and not necessarily to solve constrained TV-minimization. As there is no proof of convergence for ASD-POCS, we have derived necessary conditions for convergence (Sidky and Pan 2008). First, the image constraints must be satisfied:  $\mathbf{f} \geq \mathbf{0}$  and  $D(\mathbf{f}) \leq \epsilon$ . The latter constraint is satisfied with equality, because the zero-TV image lies outside the data tolerance constraint if there is something in the CBCT scanner. Second, there is a parameter  $c_\alpha$ , which can be computed from an image estimate (Sidky and Pan 2008). Physically, this parameter is the cosine of an angle in the  $N$ -dimensional space of images; this angle lies between the gradient vectors of the data divergence and image TV, and these vectors should be back to back or, equivalently,  $c_\alpha$  should be  $-1$ , at the solution to equation (3). Due to the high dimensionality of the space of images,  $c_\alpha$  is a quite sensitive



parameter, and it has been our experience that, with actual scanner data, changes to the image estimate become imperceptible when  $c_\alpha < -0.5$  and the image constraints are satisfied.

In this study, a modification was made to the ASD-POCS algorithm for improving its convergence in solving the constrained optimization problem in equation (3). This modification involves employing the POCS step to reduce the data divergence until about 80 iterations, after which gradient descent is employed for reducing the data-divergence. With this modification, accurate solutions to equation (3) are obtained within 200 iterations. We point out that this ASD-POCS algorithm is developed in the spirit of a plug-and-play algorithm, as discussed in Pan *et al* (2009), and contains adaptive steps that make proof of convergence quite difficult, if not impossible. On the other hand, resulting images are checked against the necessary optimality conditions:  $c_\alpha = -1$ ,  $\mathbf{f} \geq \mathbf{0}$  and  $D(\mathbf{f}) = \epsilon$ .

The motivation for solving equation (3) accurately is twofold: (1) for a given system matrix  $\mathcal{H}$  and data set  $\mathbf{g}$ , the reconstructed image is only a function of  $\epsilon$ , and (2) assuming that an ERP exists for CBCT, the solution to equation (3) may be highly accurate for small  $\epsilon$ . Small  $\epsilon$  constrains the possible images so that the estimated data agree closely with the available data. In general,  $\epsilon$  must be larger than 0 in order for there to be a feasible image because of inconsistency between the actual data and the system model. Relaxing  $\epsilon$  (going to larger values) includes images with lower TV, thereby allowing for greater TV regularization. The spirit of CS-style image reconstruction involves solving equation (3) for small  $\epsilon$ , which is technically challenging. Note that, with ideal data, CS calls for solving equation (3) with  $\epsilon = 0$ . The idea is that the sparse-view sampling has a large null space, where many images could agree with the available data within a small  $\epsilon$ . If an ERP exists for the system matrix, one can expect that the minimum-TV image with a tight  $\epsilon$  could accurately represent the underlying object function. Indeed, it is likely that many over-regularized, blocky images, which arise from TV regularization, correspond to solving equation (3) with too large an  $\epsilon$ . The POCS-data divergence provides a lower bound of  $\epsilon$ , and we select a final  $\epsilon$  in the neighborhood of the bound.

#### 4. Performance evaluation of image reconstruction

The performance of various TV-minimization-based algorithms in CT-image reconstruction has been evaluated in simulation studies (Sidky *et al* 2006, Sidky and Pan 2008, Leng *et al* 2008, Herman and Davidi 2008). The focus of the work reported here is on the evaluation of the ASD-POCS algorithm with real CBCT data in imaging experiments of potential practical significance. We also implemented the POCS and EM algorithms in order to establish a relative performance benchmark for the ASD-POCS algorithm. It should be pointed out that additional, different algorithms may be devised for solving the optimization problems mentioned in sections 3.2 and 3.3 and that additional, different optimization formulations and the associated algorithms may be devised for image reconstruction based upon the imaging model in equation (1). It is possible that these algorithms may yield potentially improved reconstruction. However, research on these optimization formulations and algorithms is beyond the scope of this work.

##### 4.1. Qualitative-visualization-based evaluation

In this study, we first conducted a qualitative evaluation by using visual inspection and comparison of reconstructed images. To reveal the structure and contrast details in a reconstruction, we also display selected regions of interest (ROIs) with a narrowed display grayscale and/or zoomed-in view. Although visual inspection of images provides only a

qualitative comparison of algorithm performance, it can be an informative assessment of the image quality especially in the presence of image artifacts that are otherwise difficult to quantify meaningfully using general metrics. Images were displayed with separate grayscale windows to facilitate bone or soft-tissue visualization. When a narrow grayscale window is used, it may reveal considerable reconstruction artifacts that may be otherwise invisible in a wide grayscale window. In our study, we have used grayscale windows that are consistent between images reconstructed using different algorithms for purpose of comparison.

#### 4.2. Quantitative-metric-based evaluation

It is well recognized that image quality is multiple faceted, depending upon the tasks for which images are reconstructed. This is particularly true in real-data studies in which the ‘truth’ about the underlying object function is unknown. To evaluate different aspects of image quality in real-data studies under consideration, we also use a number of technical-efficacy-based metrics, which are illustrated below.

**4.2.1. Image-similarity metrics.** Currently, in a practical application of CBCT, an image,  $\mathbf{f}_0 = (f_{01}, f_{02}, \dots, f_{0N})^T$ , is reconstructed from full data using the FDK algorithm with a Hann filter, which is used as a surrogate truth. We first evaluate quantitatively the reconstruction quality by considering the following two metrics: universal quality index (UQI) (Wang and Bovik 2002) and mutual information (MI) (Pluim *et al* 2003), which can be used for measuring the degree of similarity between the reconstructed and FDK-reference images. It should be pointed out that the FDK-reference image  $\mathbf{f}_0$  is not the real ‘truth’, and as discussed in section 7 below, the use of different reference images in the computation of image-similarity metrics can lead to quantitatively different evaluation results. We use  $\mathbf{f}_1 = (f_{11}, f_{12}, \dots, f_{1N})^T$  to denote an image reconstructed from sparse-view data.

For a selected ROI within the reconstructed and reference images, we define image means, variances and covariances over an ROI as

$$\bar{f}_j = \frac{1}{N'} \sum_{n=1}^{N'} f_{jn}, \quad \sigma_j^2 = \frac{1}{N' - 1} \sum_{n=1}^{N'} (f_{jn} - \bar{f}_j)^2, \quad (4)$$

where  $j = 0$  and  $1$ , and

$$\text{Cov}\{\mathbf{f}_1, \mathbf{f}_0\} = \frac{1}{N' - 1} \sum_{n=1}^{N'} (f_{1n} - \bar{f}_1)(f_{0n} - \bar{f}_0), \quad (5)$$

where  $N'$  denotes the number of voxels within the ROI.

Using equations (4) and (5), the UQI is defined as

$$\text{UQI} = \frac{2\text{Cov}\{\mathbf{f}_1, \mathbf{f}_0\}}{\sigma_1^2 + \sigma_0^2} \frac{2\bar{f}_1\bar{f}_0}{\bar{f}_1^2 + \bar{f}_0^2}; \quad (6)$$

UQI measures the pixel-to-pixel similarity between the reconstructed and reference images, and its value ranges between 0 and 1. The closer to 1 the UQI value, the more similar to the reference image the corresponding reconstruction.

When reconstructed and reference images are interpreted as ‘stochastic processes’, the MI between them can be used for measuring their mutual dependence:

$$\text{MI}\{\mathbf{f}_1, \mathbf{f}_0\} = \sum_{n=1}^{N''} \sum_{n'=1}^{N''} p(f_{1n}, f_{0n'}) \log \left( \frac{p(f_{1n}, f_{0n'})}{p(f_{1n}) p(f_{0n'})} \right), \quad (7)$$



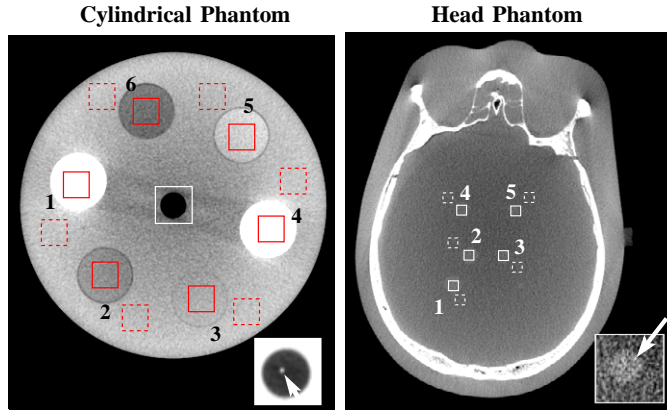


**Figure 2.** s-ROIs (solid-line squares) and b-ROIs (dashed-line squares) selected within transverse slices at  $z = 2.0$  cm in the cylindrical phantom (left) and  $z = 1.2$  cm in the head phantom (right) for CNR computation. The ROIs in the cylindrical phantom correspond to cortical bone (ROI 1 and ROI 4) and breast (ROI 2), brain (ROI 3), liver (ROI 5) and adipose (ROI 6) tissues. The cylindrical and head phantom images are displayed with soft-tissue-grayscale windows of  $[-257, 143]$  HU and  $[-429, 429]$  HU. The wire insert in the central region of the cylindrical phantom and ROI 2 of the head phantom, which are displayed with a zoomed-in view using grayscale windows of  $[-1000, -143]$  HU and  $[-200, 28]$  HU, are used as the signals for the detectability calculation. Cupping artifacts can be observed as a result of physical factors, such as beam-hardening and scatter, when the image is displayed with a narrow grayscale window.

where the ‘marginal densities’  $p(f_{1n})$  and  $p(f_{0n})$  are determined using the corresponding histograms of  $\mathbf{f}_1$  and  $\mathbf{f}_0$ , whereas the joint density  $p(f_{1n}, f_{0n'})$  is estimated from a 2D joint histogram of  $\mathbf{f}_1$  and  $\mathbf{f}_0$ , and  $N''$  denotes number of bins in the histogram. We normalized the MI by the MI of the reference image and refer to the normalized MI simply as MI afterward. Unlike UQI, which measures the pixel-to-pixel dependence of a reconstructed image on the reference image, MI measures the histogram correlation between them. As such, it can be highly sensitive to small differences between visually similar images (Pluim *et al* 2003). The higher the similarity-metric values, the higher the degree of similarity of the reconstructed images to the reference image.

**4.2.2. Contrast-to-noise ratio.** The contrast-to-noise ratio (CNR) is a metric commonly used for evaluation of image contrast and noise properties within a selected ROI relative to its background ROI. For the computation of CNR, we select two ROIs of the same size, which contain the low-contrast structures and background, and refer to them as the s-ROI and b-ROI. The CNR is defined as

$$\text{CNR} = \frac{2|\bar{f}^{(s)} - \bar{f}^{(b)}|}{\sigma^{(s)} + \sigma^{(b)}}, \quad (8)$$

where  $\bar{f}^{(s)}$  and  $\sigma^{(s)}$ , or  $\bar{f}^{(b)}$  and  $\sigma^{(b)}$ , denote the mean and standard deviation over the s-ROI, or b-ROI, which are computed using equation (4). For the cylindrical phantom, as shown in figure 2, the solid-line square embedded in, and the dashed-line square near, an insert indicate the s-ROI and the corresponding b-ROI. As figure 2 shows, the head phantom contains several low-contrast objects mimicking tumors of different sizes and locations. Again, the solid-line square embedded in, and the dashed-line square near, a low-contrast object indicate an s-ROI and its corresponding b-ROI. We calculate below CNR between each pair of the s- and b-ROIs.

#### 4.3. Image-power-spectrum evaluation

Recognizing the distinction from a true ‘noise-power spectrum’ (NPS) (Burgess and Judy 2007, Metheany *et al* 2008, Gang *et al* 2010) in the characterization of noise magnitude and correlation in statistically stationary images, we define below a power spectrum ( $P_c$ ) measured directly from the image reconstruction in otherwise homogeneous ROIs. While  $P_c$  does not strictly obey assumptions of shift invariance and noise stationarity, among others, as the NPS, it provides a useful, quantitative, relative metric of noise magnitude and correlation among the various algorithms for sparse-view reconstruction under consideration. In order to calculate the image fluctuations in a small ROI within a reconstructed image, we select  $L$  square-shaped ROIs of equal size at different locations within the image. Each of the ROIs is within the support of the entire image and in the homogeneous region of the image, and each ROI can overlap with other ROI but not more than half of its size. The image-power spectrum on a Cartesian grid is defined as

$$P_c(\mathbf{k}) = \frac{1}{L} \sum_{l=1}^L |\text{DFT}\{\mathbf{W}(\mathbf{f}_l - \mathbf{f}_{\text{ave}})\}|^2, \quad (9)$$

where ‘DFT’ denotes the discrete Fourier transform (DFT),  $\mathbf{k}$  the discrete frequency vector,  $\mathbf{f}_l$  is the image within the  $l$ th ROI,  $\mathbf{f}_{\text{ave}}$  is the mean ROI image and each of its elements represents the average of the values at the same voxel within different ROI images, and  $\mathbf{W}$  is a discrete window function for reducing excessive power at the edges of the ROI (Percival and Walden 1993). In the evaluation study below, we first calculated image power spectra  $P_c(\mathbf{k})$  for selected 2D ROIs and then converted power spectra  $P_c(\mathbf{k})$  onto a polar grid, followed by averaging them over the polar angle to obtain power spectra  $P_p(k)$  as functions only of discrete radial frequencies  $k$ .

#### 4.4. Detection-task-based evaluation

We also carried out an evaluation study on algorithm performance by using a model observer in a detection task. The detectability index of the model observer is defined as

$$d'^2 = \sum_{\mathbf{k}} \frac{|S(\mathbf{k})|^2}{P_c(\mathbf{k})}, \quad (10)$$

where  $S(\mathbf{k})$  denotes the DFT of the signal, and  $P_c(\mathbf{k})$  the power spectrum of the background. This model observer is similar to the widely used pre-whitening observer, recognizing that analysis from measured data here does not strictly obey the rigorous assumptions of linearity and shift invariance, among other conditions (ICRU, 1996, Burgess *et al* 2001, Burgess and Judy 2007). Nevertheless,  $d'$  provides a quantitative metric of relative comparison in task performance among the various sparse-view reconstructions below (Siewerdsen and Jaffray 2000, Gang *et al* 2010, Reiser and Nishikawa 2010). Superficially, it appears that CNR and  $d'$  measure similar quantities, but there is a significant difference in how the statistical model of the image enters in these quantities. CNR includes only the estimated image variance in the denominator, while  $d'$  accounts for some measure of the image covariance.

In the study below, the ‘signal’ (i.e. the numerator in equation (10)) are the high contrast wire in the cylindrical phantom, highlighted by a small arrow in the square box at the lower-right corner in the left panel of figure 2, and the low-contrast, extended tumor in the head phantom, displayed at the lower-right corner in the right panel of figure 2. We applied signal masks

obtained by using the corresponding FDK-reference images to determining signal regions within reconstructed images. A signal image was subsequently obtained by subtracting from the reconstruction within the determined signal region a background image estimated from a region surrounding the signal region. From the obtained signal image, we subsequently computed the image-energy spectrum  $S(\mathbf{k})$ . The background power spectra were determined as described in section 4.3 above. Using the computed  $|S(\mathbf{k})|^2$  and  $P_c(\mathbf{k})$  in equation (10), we then obtained the detectability indices for reconstructed images. The ‘signal’ numerator of equation (10) therefore corresponds to spatial-frequency-dependent tasks for (i) detection of the wire, which emphasizes higher frequency structures and (ii) detection of the low-contrast simulated lesion, which emphasizes lower frequency structures.

## 5. Experimental study of the cylindrical phantom

For the cylindrical phantom, we collected full data at 960 views uniformly distributed over  $2\pi$ . From the full data set, we extracted data sets containing 15, 30, 60 and 96 views evenly distributed over  $2\pi$  and refer to them as the 15-, 30-, 60- and 96-view data sets. From the full and sparse-view data sets, images were reconstructed with a voxel size of 0.05 cm. For the ASD-POCS algorithm, the average values of  $\epsilon$  per ray measurement were chosen to be about  $8.2 \times 10^{-6}$ ,  $5.6 \times 10^{-6}$ ,  $3.9 \times 10^{-6}$  and  $3.2 \times 10^{-6}$  for the 15-, 30-, 60- and 96-view data sets, respectively.

### 5.1. Qualitative visual evaluation

Using the FDK, EM, POCS and ASD-POCS algorithms, we reconstructed images from sparse-view data sets and displayed in figures 3 and 4 transverse, sagittal and coronal images reconstructed from 30- and 60-view data sets, respectively, with bone- and soft-tissue-grayscale windows. As the results show, image differences of different view numbers or different algorithms are more evident when displayed in a narrow grayscale window. In general, images reconstructed with the ASD-POCS algorithm appear visually more similar to the FDK-reference images than the other algorithms.

The low-contrast inserts can be distinguished with the number of views as low as 30 for images reconstructed using the ASD-POCS algorithm, as shown in figure 4. It is also interesting to observe that the high contrast wire in the FOV center was recovered well in both 30- and 60-view FDK-reconstruction images. On the other hand, although the EM and POCS images have less streak artifacts, it is more difficult to observe the wire in the images. This is understandable because the wire is near the FOV center, where it can be sufficiently sampled by a small number of views, thus allowing reasonably accurate FDK reconstruction of the wire. This observation suggests that depending on the task, the FDK algorithm can also perform well when applied to sparse-view data. The wire image obtained with the ASD-POCS algorithm seems to have a contrast level higher than that of the wire in the FDK-reference images, as shown in figure 4. It should be noted that, when images are displayed in a narrow grayscale window, some cupping artifacts can be observed that are caused largely by beam-hardening and x-ray scatter.

### 5.2. Quantitative-metric-based evaluation

We have also carried out quantitative evaluation studies using the metrics described in section 4.2.

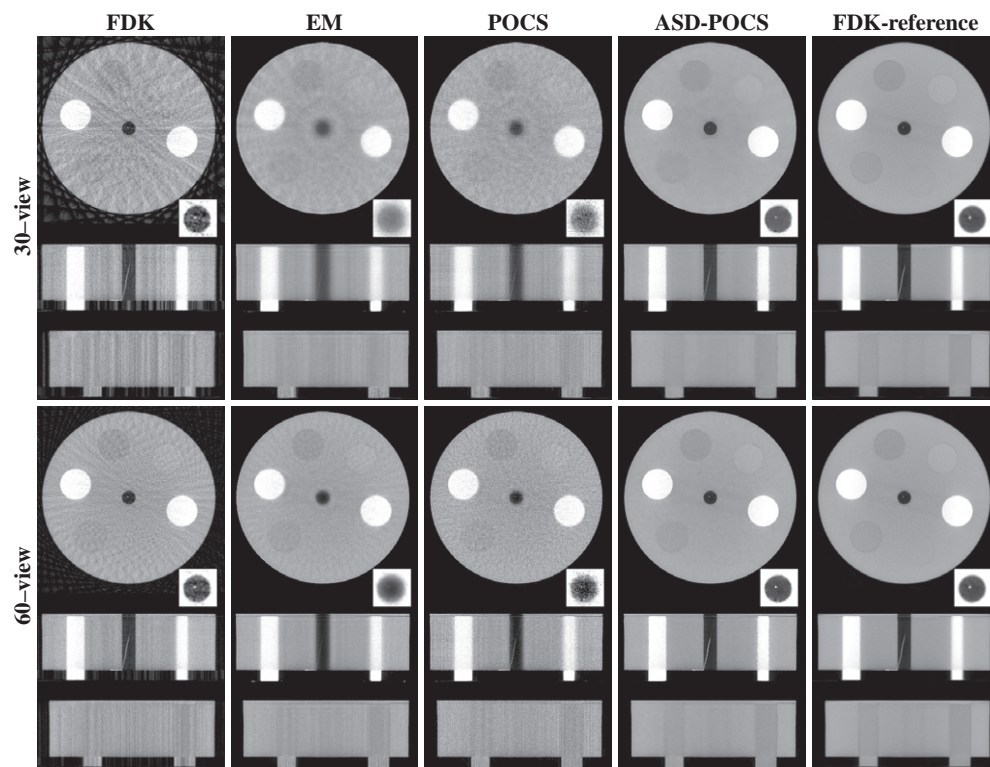


**Figure 3.** Images of the cylindrical phantom reconstructed from 30-view (rows 1-3) and 60-view (rows 4-6) data sets using the FDK, EM, POCS and ASD-POCS algorithms, within a transverse slice at  $z = 2.0$  cm (rows 1 and 4), coronal slice at  $x = -3.0$  cm (rows 2 and 5) and sagittal slice at  $y = -0.25$  cm (rows 3 and 6). The central region of the transverse slice is re-displayed with a zoomed-in view using a grayscale window of  $[-1000, -143]$  HU to show the wire insert. The last column is the FDK-reference images within the corresponding slices. A bone grayscale window,  $[-1000, 714]$  HU, is used.

**5.2.1. Similarity-metrics evaluation.** In figure 5, we display UQI and MI computed from reconstructed images of the cylindrical phantom. Also, results similar to those described above were obtained for different ROIs. The results suggest that the ASD-POCS algorithm yields images more similar to the FDK-reference image than do other algorithms under the study. The FDK results increase rapidly as the number of views increases. As elaborated in section 7 below, this is attributable to the fact that the FDK-reference image was used in the computation of similarity metrics. When the number of views increases, the FDK reconstruction becomes rapidly similar to the FDK-reference image.

**5.2.2. CNR-metric-based evaluation.** For the selected s- and b-ROIs in the cylindrical phantom, as shown in figure 2, we calculated CNR using equation (8) and plot the results, as functions of the projection views in figure 5 for pair 6 of s- and b-ROIs, corresponding to the ‘adipose tissue’ inserts. For comparison, we also calculated the CNR for the corresponding ROIs within the FDK-reference image and plot them as the dashed lines. CNR obtained with the ASD-POCS algorithm appears higher than those obtained with other algorithms. This is because the ASD-POCS algorithm generally yields images with a noise level lower than other

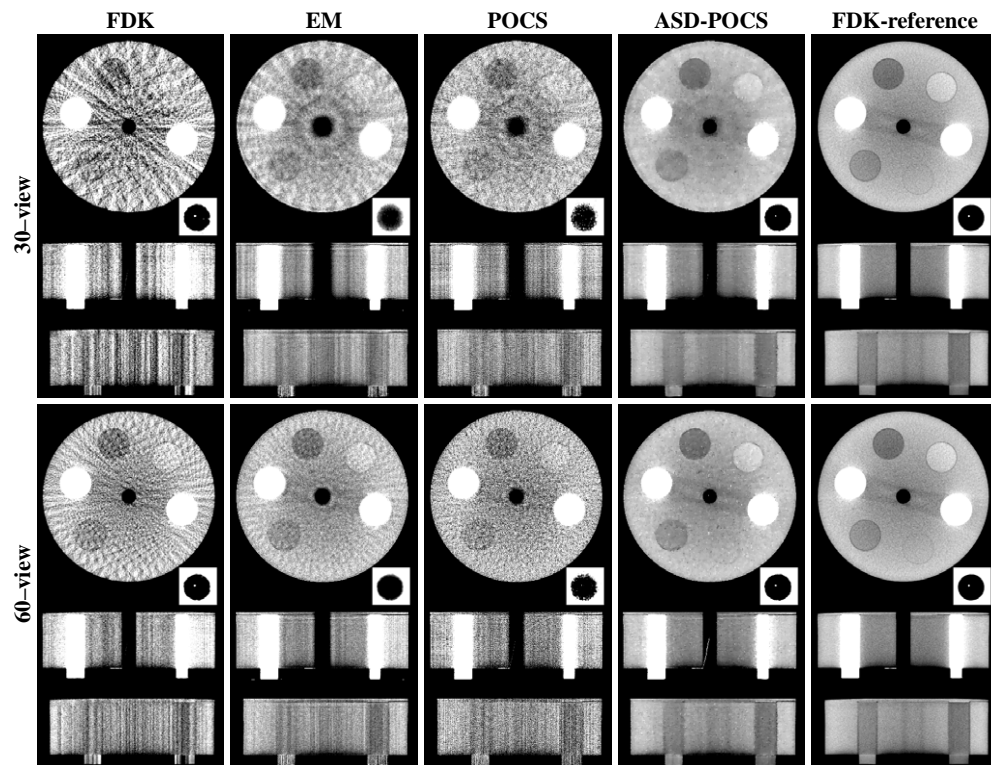


**Figure 4.** Images of the cylindrical phantom reconstructed from 30-view (rows 1-3) and 60-view (rows 4-6) data sets using the FDK, EM, POCS and ASD-POCS algorithms, within a transverse slice at  $z = 2.0$  cm (rows 1 and 4), coronal slice at  $x = -3.0$  cm (rows 2 and 5) and sagittal slice at  $y = -0.25$  cm (rows 3 and 6). The central region of the transverse slice is re-displayed with a zoomed-in view using a grayscale window of  $[-571, -429]$  HU to show the wire insert. The last column is the FDK-reference images within the corresponding slices. A soft-tissue grayscale window,  $[-257, 143]$  HU, is used.

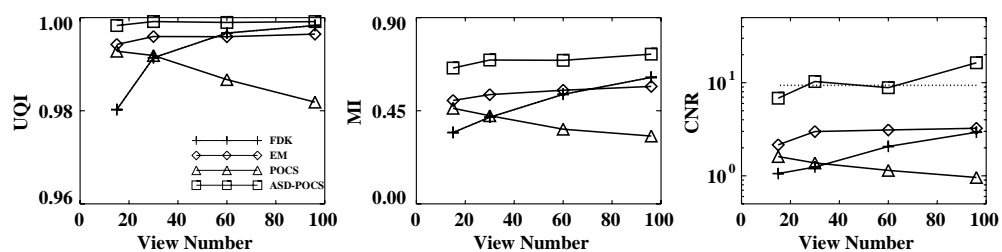


**Figure 5.** UQI (left), MI (middle) and CNR (right) as functions of projection views, computed from the cylindrical phantom images reconstructed using the FDK (+), EM ( $\times$ ), POCS ( $\Delta$ ) and ASD-POCS ( $\square$ ) algorithms and the FDK-reference image. The dotted line displays the corresponding CNR in the FDK-reference image.

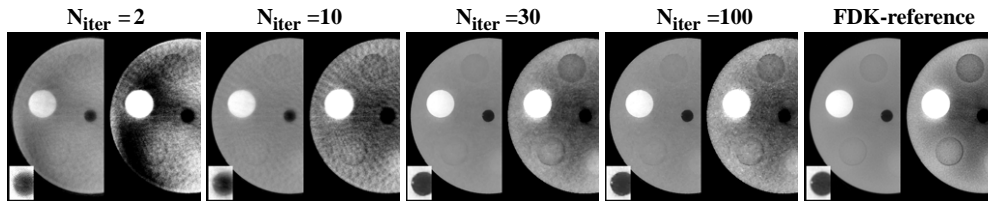


**Figure 6.** ROI images of the cylindrical phantom within a transverse slice at  $z = 0$  cm reconstructed from 60-view data using the ASD-POCS algorithm at iterations 2, 10, 30 and 100. For each displayed iteration number, the ROI image is shown with a bone-grayscale window  $[-1000, 714]$  HU (left) and a soft-tissue-grayscale window  $[-257, 143]$  HU (right). The square ROI shows the zoomed-in view of the central region containing the wire with a grayscale window  $[-1000, -143]$  HU.

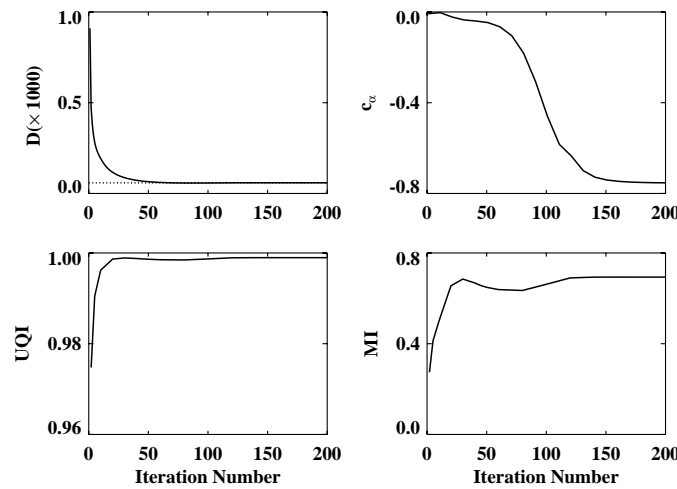


**Figure 7.** Image-property parameters, as functions of iteration numbers for images reconstructed from 60-view data using the ASD-POCS algorithm. Row 1: data divergence  $D$  (left) and parameter  $c_\alpha$  (right), and row 2: UQI (left) and MI (right) calculated within the entire image support. The dotted line in data-divergence plot indicates the selected  $\epsilon$ .

algorithms under the study. Similar CNR results were also obtained for other pairs of s- and b-ROIs in reconstructed images.

**5.2.3. Image properties as functions of iteration numbers.** We also studied the evolution of image reconstruction as functions of iterations in the EM, POCS and ASD-POCS algorithms. In figure 6, we display ROI images containing the low-contrast structures within the slice at  $z = 0$  cm reconstructed from the 60-view data using the ASD-POCS algorithm at iterations 2, 10, 30 and 100, with different grayscale windows for showing reconstruction details. Visual inspection of the results suggests that images with reasonable quality can be reconstructed even at early iterations. To assess quantitatively the reconstruction as a function of iterations, we also calculated data divergence, convergence parameter  $c_\alpha$  and quantitative metrics such as UQI and MI for different iterations. The quantitative results, as shown in figure 7, corroborate the observation that the ASD-POCS algorithm seems to be able to reconstruct images of reasonable quality at an early stage of the iteration.



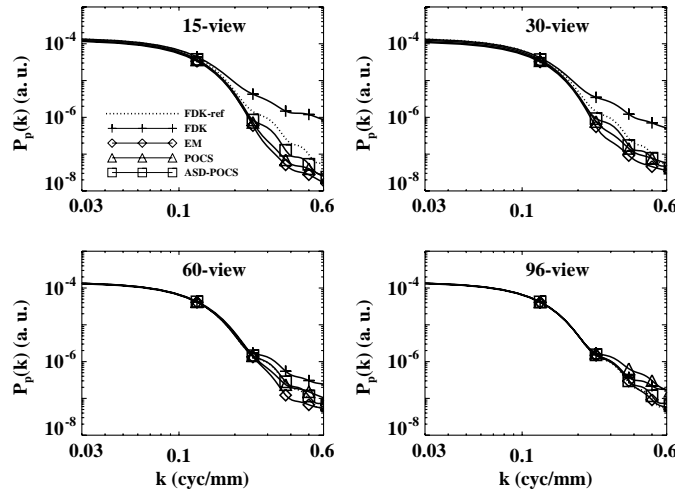


**Figure 8.** Power spectra of the cylindrical phantom obtained from 15-, 30-, 60- and 96-view data sets using the FDK (+), EM ( $\diamond$ ), POCS ( $\triangle$ ) and ASD-POCS ( $\square$ ) algorithms. The power spectrum of the FDK-reference image is plotted as the dotted curve.

### 5.3. Power-spectrum-metric-based evaluation

For the cylindrical phantom experiment, as described in section 4.3, we calculated the power spectra  $P_p(k)$  using 25  $40 \times 40$  selected ROIs within a 2D image at  $z = 0$  cm and display them in figure 8. For comparison, we also calculated the corresponding power spectrum of the FDK-reference image and display it as the dotted curve. The power spectra obtained using the FDK, EM and POCS algorithms agree well with the reference power spectrum at low frequencies, although the former differs from the latter at high frequencies. This is consistent with the ‘streakiness’ observed in the images. The result of the ASD-POCS algorithm agree well with the reference power spectrum over a frequency range wider than those of the other algorithms.

### 5.4. Detection-task-based evaluation

We computed, using equation (10), the model-observer detectabilities for the high contrast wire in reconstructed cylindrical-phantom images and display them in figure 9 as functions of projection views and iteration numbers. For the latter case, images at different iterations were reconstructed from 60-view data set using the EM, POCS and ASD-POCS algorithms. The results suggest that the ASD-POCS algorithm generally yields a detectability higher than do the other algorithms in terms of the detection task described. We have also computed the detectability indices for reconstructions from other sparse-view data sets, and observations similar to those described above can be made.

The following study on a physical head phantom serves as further demonstration and evaluation of the ASD-POCS algorithm, and the complexity of the phantom provides added significant challenge to the constrained TV-minimization.

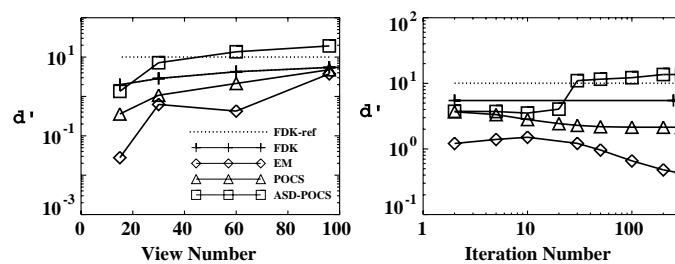


**Figure 9.** Detectabilities for the wire as functions of projection views (left) and iteration number (right) calculated from cylindrical phantom images reconstructed using the FDK (+), EM ( $\diamond$ ), POCS ( $\triangle$ ) and ASD-POCS ( $\square$ ) algorithms. The detectability of the FDK-reference image is plotted as dotted lines.

## 6. Experimental study of the anthropomorphic head phantom

For the anthropomorphic head phantom, a full data set was collected at 960 views uniformly distributed over  $2\pi$ . From the full data set, we extracted data sets containing 15, 30, 60 and 96 views evenly distributed over  $2\pi$  from which we subsequently reconstructed images with a voxel size of 0.045 cm. For the ASD-POCS algorithm, the average values of  $\epsilon$  per ray measurement were chosen to be about  $3.2 \times 10^{-5}$ ,  $2.4 \times 10^{-5}$ ,  $1.7 \times 10^{-5}$  and  $1.3 \times 10^{-5}$  for 15-, 30-, 60- and 96-view data sets, respectively.

### 6.1. Qualitative-visualization-based evaluation

We reconstructed images from the sparse-view data sets of the head phantom and display reconstructions from the 60- and 96-view data sets with a bone- and soft-tissue-grayscale windows in figures 10 and 11. The corresponding FDK-reference images are also displayed in the last columns. Observations similar to those for the cylindrical phantom images can be made. Additionally, low-contrast, small spheres mimicking brain tumors in the head phantom can be observed in the transverse and sagittal slices of the FDK-reference image. Although it is difficult to distinguish them in the FDK, EM and POCS images, they can be discerned in the ASD-POCS reconstructions, suggesting that the ASD-POCS algorithm may not only suppress image artifacts but also retain low-contrast structures. For further visualization of reconstruction details, we show in figure 12 the nasal region of the head phantom in a zoomed-in view, using different grayscale windows, reconstructed from 60- and 96-view data. The ASD-POCS algorithm seems to be able to pick up some of the subtle structures that are observed in the FDK-reference image.

### 6.2. Quantitative-metric-based evaluation

**6.2.1. Similarity-metrics-based evaluation.** In figure 13, we show UQI, and MI, as functions of projection views, computed from reconstructed images of the head phantom. UQI and MI for different ROIs within the head phantom similar to those described above were also obtained. Based upon the results, observations similar to those for the cylindrical phantom can also be made for the head phantom.

**6.2.2. CNR-metric-based evaluation.** For the selected s- and b-ROIs shown in figure 2, we calculated CNR using equation (8). In row 4 of figure 13, we display the CNR results as functions of projection views for pair 2 of s- and b-ROIs. For comparison, we also calculated



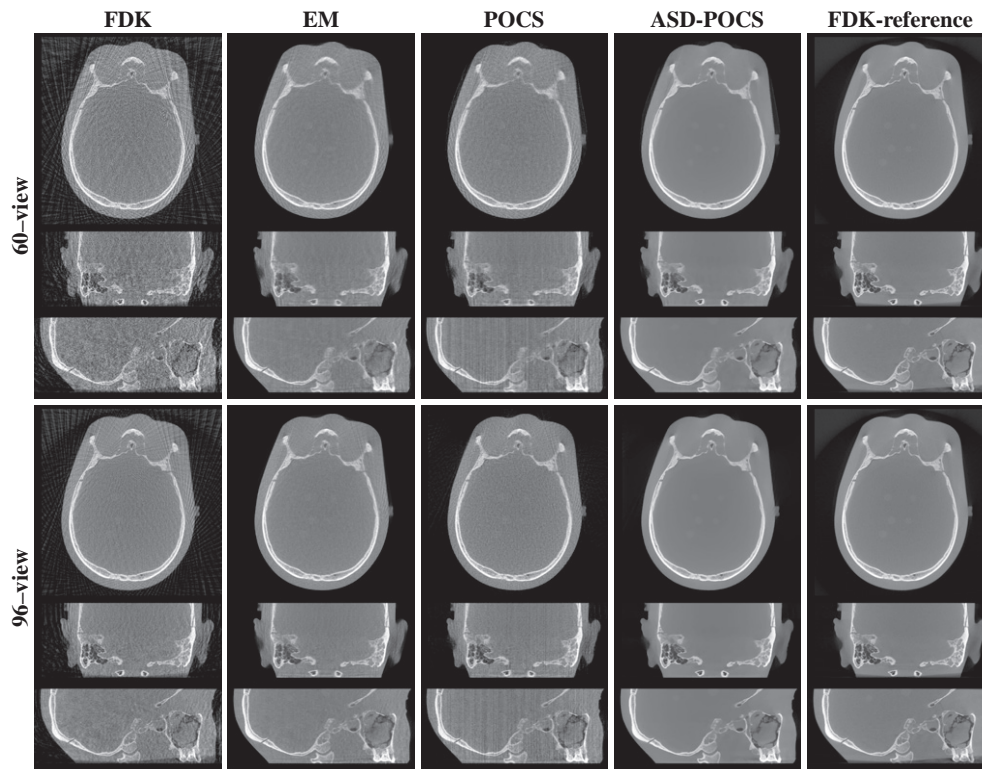


**Figure 10.** Images of the head phantom reconstructed from 60-view (rows 1-3) and 96-view (rows 4-6) data sets using the FDK, EM, POCS and ASD-POCS algorithms, within a transverse slice at  $z = 1.2$  cm (rows 1 and 4), coronal slice at  $x = 0.6$  cm (rows 2 and 5) and sagittal slice at  $y = 2.5$  cm (rows 3 and 6). The last column displays the FDK-reference images within the corresponding slices. A bone grayscale window,  $[-1000, 1000]$  HU, is used.

the CNR of the FDK-reference image and plot it as a dotted line in figure 13. Similar CNR results were also obtained for other pairs of s- and b-ROIs in the head phantom. Again, observations about algorithm performance similar to those for the cylindrical phantom can be made for the head phantom.

**6.2.3. Image properties as functions of iteration numbers.** In figure 14, we display ROI images within a transverse slice at  $z = 0$  cm reconstructed using the ASD-POCS algorithm from 96-view data at iterations 2, 10, 30 and 100. The ROI images containing the nasal region were selected and displayed in a zoomed-view with bone- and soft-tissue-grayscale for revealing reconstruction details. Visual inspection of the images suggest that images with reasonable quality can be reconstructed even at early iterations. We have also calculated data divergence  $D$ , convergence parameter  $c_\alpha$  and quantitative metrics UQI and MI at different iterations in which the convergence behavior of the ASD-POCS algorithm similar to that in figure 7 can be observed.

### 6.3. Power-spectrum-metric-based evaluation

As described in section 4.3, we selected 42  $40 \times 40$  ROIs within a 2D image at  $z = 0$  cm to calculate the power spectra  $P_p(k)$  and display them in figure 8. The selected ROIs are within

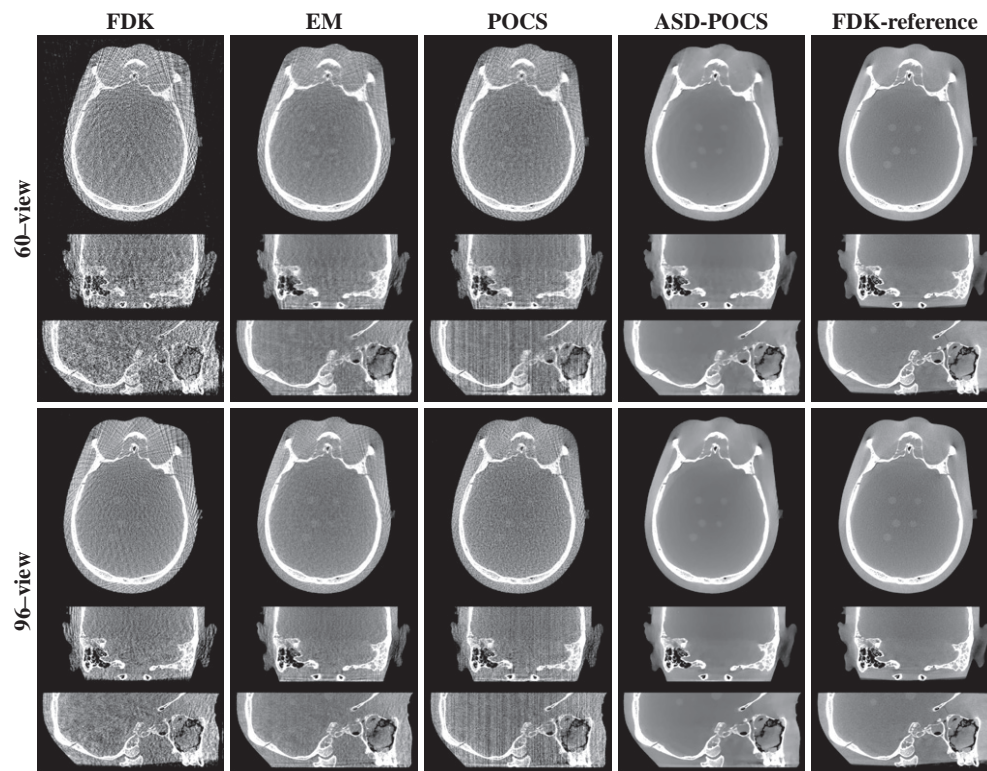


**Figure 11.** Images of the head phantom reconstructed from 60-view (rows 1–3) and 96-view (rows 4–6) data sets using the FDK, EM, POCS and ASD-POCS algorithms, within a transverse slice at  $z = 1.2$  cm (rows 1 and 4), coronal slice at  $x = 0.6$  cm (rows 2 and 5) and sagittal slice at  $y = 2.5$  cm (rows 3 and 6). The last column displays the FDK-reference images within the corresponding slices. A soft-tissue grayscale window,  $[-429, 429]$  HU, is used. Low-contrast tumor structures can be observed in the ASD-POCS reconstructions and FDK-reference images.

the brain region and have no overlap with the bones in the outer regions of the head. For comparison, the corresponding power spectrum of the FDK-reference image is also displayed as the dotted curve. The general trends of the power spectra obtained for different data sets and different algorithms are consistent with those for the cylindrical phantom.

#### 6.4. Detection-task-based evaluation

We also computed detectabilities in equation (10) for the low-contrast lesion in reconstructed head-phantom images, which are shown in figure 16 as functions of projection views and iteration numbers. For the latter case, images at different iterations were reconstructed from 96-view data set. The results suggest that the ASD-POCS algorithm generally yields a detectability higher than do the other algorithms in terms of the detection task described. We have computed detectability indices for reconstructions from other sparse-view data sets, and observations similar to those described above can be made.

### 7. Comments on the numerical results

The overall summary of the results indicates that image-reconstruction algorithms solving constrained TV-minimization can be effective at significantly reducing streak artifacts when

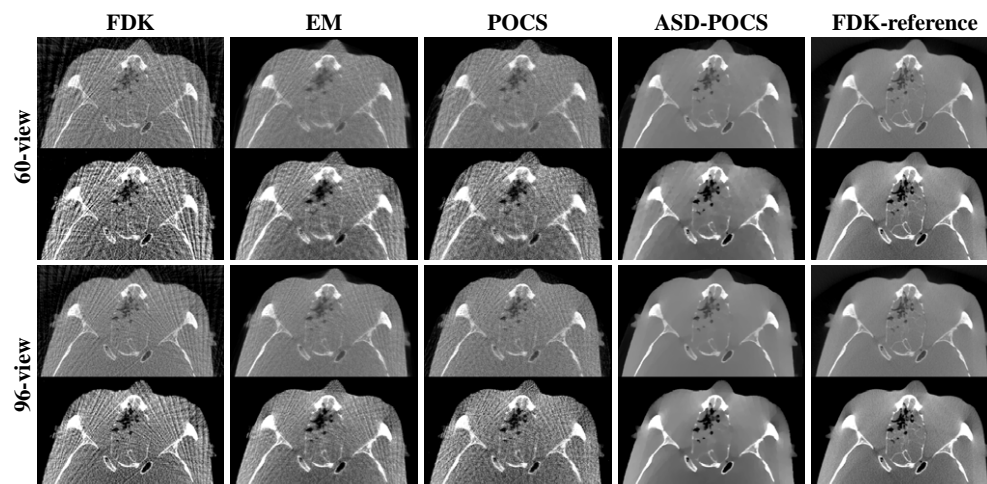


**Figure 12.** Nasal-region images of the head phantom within a transverse slice at  $z = 0$  cm reconstructed from 60-view (row 1-2) and 96-view (row 3-4) data sets using the FDK, EM, POCS and ASD-POCS algorithms displayed in a bone grayscale window of  $[-1000, 1000]$  HU (row 1 and 3) and a soft-tissue grayscale window of  $[-429, 429]$  HU (row 2 and 4). The corresponding FDK-reference images are shown in the last column.

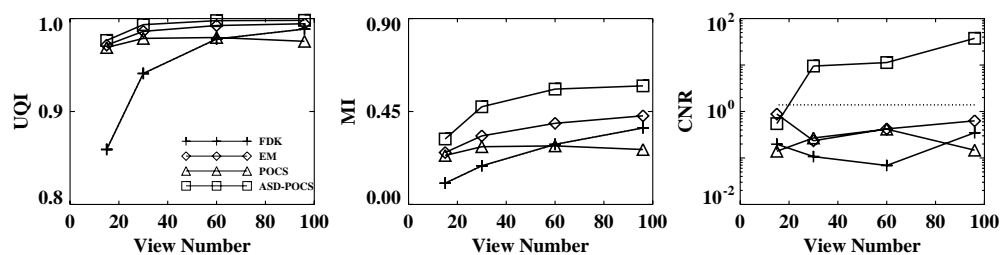


**Figure 13.** UQI (left), MI (middle) and CNR (right) as functions of projection views, computed from the head phantom images reconstructed using the FDK (+), EM (◇), POCS (△) and ASD-POCS (□) algorithms and the FDK-reference image. The dotted line displays the corresponding CNR in the FDK-reference image.

CBCT projections are taken at a limited number of views. The comparisons have been quantified using metrics sensitive to different aspects of image quality, and in each case the ASD-POCS algorithm generally yields numbers similar to the FDK-reference image. A notable exception is the MI metric, which measures the histogram correlation between two images. Clearly, it is more sensitive than some other metrics in detecting image differences. For data sets containing more than 30 views, the signal-detection metrics appear to be larger than the FDK-reference. As each of these metrics is a ratio of some measure of the reconstructed signal and the image noise, the larger values for CNR and  $d'$  reflect the fact that the signal can be reconstructed while the background is effectively de-noised.

A few words on constrained TV-minimization and the ASD-POCS algorithm are in order. One of the themes of this work is to demonstrate that the optimization problem of constrained TV-minimization, suggested in the CS field, is of interest to image reconstruction with actual CBCT data. The skeptical reader might note that the cylindrical phantom seems

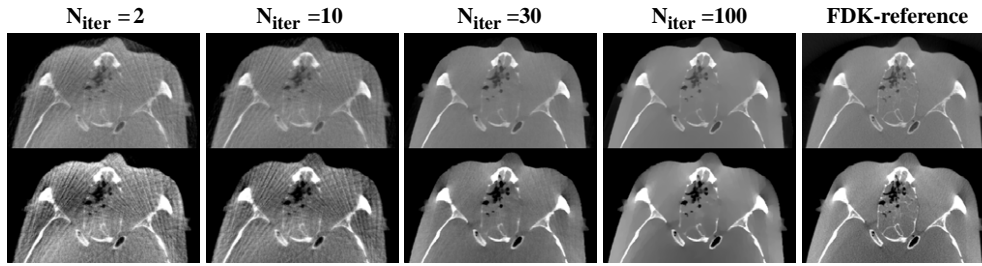


**Figure 14.** Nasal-region images of the head phantom within a transverse slice at  $z = 0$  cm reconstructed from 96-view data using the ASD-POCS algorithm at iterations 2, 10, 30 and 100, displayed with a bone-grayscale window  $[-1000, 1000]$  HU (row 1) and a soft-tissue grayscale window  $[-429, 429]$  HU (row 2).

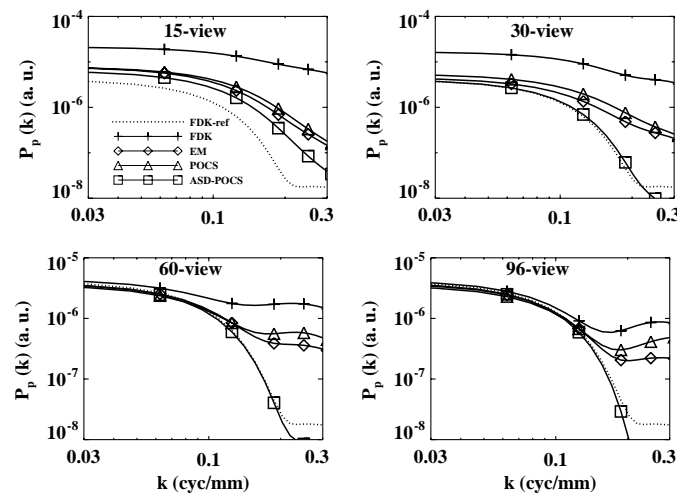


**Figure 15.** Power spectra of the head phantom obtained from 15-, 30-, 60- and 96-view data sets using the FDK (+), EM ( $\diamond$ ), POCS ( $\triangle$ ) and ASD-POCS ( $\square$ ) algorithms. The power spectrum of the FDK-reference image is plotted as the dotted curve.

to be piece-wise constant, and therefore favors the ASD-POCS algorithm for constrained TV-minimization. But we point out that actual scanner data are quite inconsistent with the discrete x-ray transform model of equation (1). Streaking and cupping from beam-hardening and x-ray scatter are visible in the FDK-reference image displayed with a soft-tissue grayscale window in figure 4. The profiles of the 60-view ASD-POCS, FDK-reference and ASD-POCS-reference images in figure 17 clearly show that the resulting images are not really piece-wise constant.

Another interesting point, which will take future investigation to clarify, is the question of whether or not the solution to constrained TV-minimization is a desirable image. The plots of  $D$  and  $c_\alpha$  in figure 7 indicate that ASD-POCS accurately solves equation (3). The plots of  $d'$  in figures 9 and 16 are quite interesting in addressing this question. Note that, for example, the EM achieves a maximum  $d'$  well short of converging to its minimizer of the KL-data divergence. As an aside, this phenomenon is well known and is not surprising because we have included no regularization with the EM implementations. (The inclusion of regularizations in the EM

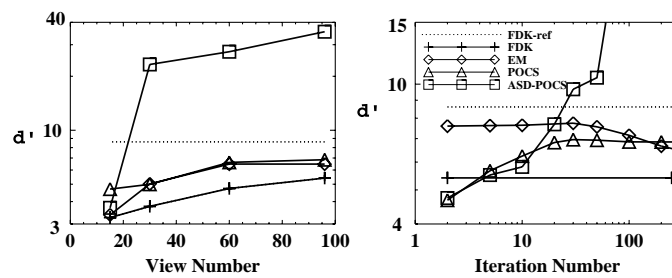


**Figure 16.** Detectabilities for the low-contrast lesions as functions of projection views (left) and iteration number (right) calculated from head phantom images reconstructed using the FDK (+), EM ( $\diamond$ ), POCS ( $\triangle$ ) and ASD-POCS ( $\square$ ) algorithms. The detectability of the FDK-reference image is plotted as dotted lines.

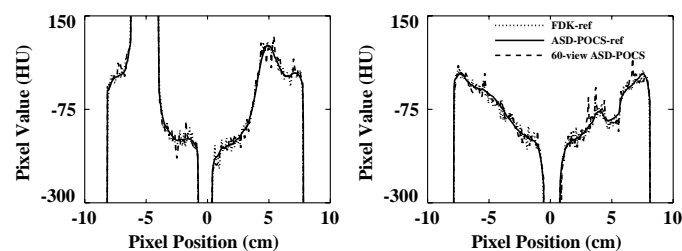


**Figure 17.** Profiles along two lines within the transverse slice at  $z = 0$  cm in the FDK- (dotted curve) and ASD-POCS-reference (solid curve) images and in the 60-view, ASD-POCS reconstruction (dashed curve) of the cylindrical phantom. It is obvious that the images are not piece-wise constant.

algorithm generally leads to a different algorithm that minimizes an objective function that is likely to differ from the pure KL-data divergence that the EM algorithm minimizes.) In contrast, the ASD-POCS algorithm appears to achieve a maximum  $d'$  when the image estimate approaches the solution to equation (3). This question is important from the standpoint of the complexity of the image reconstruction. The solution of constrained TV-minimization depends only on data, system matrix and  $\epsilon$ , while intermediate image estimates depend on, in addition to these factors, detailed parameters and implementation of the particular reconstruction algorithm.

The evaluation results can be dependent on a reference image used. In the similarity-metrics-based evaluation studies presented, it is not unreasonable to use the FDK-reference image because it is the image currently used in practical applications. However, the FDK-reference image represents only an approximate reconstruction of the underlying ‘truth’, and thus the selection of a reference image different from the FDK-reference image is likely to lead to different evaluation results. As shown in figure 1, we also include images reconstructed from full, 960-view data using the ASD-POCS algorithm. These images, which we refer to as the *ASD-POCS-reference* images, are visually highly similar to the FDK-reference images. However, a close inspection reveals differences between them: the wire in the ASD-POCS-reference image for the cylindrical phantom has higher contrast than that in the FDK-reference image, and more details in the trabecular bone of the head can be observed in the ASD-POCS-reference image than in the FDK-reference image. As shown in row 1 of figure 18,

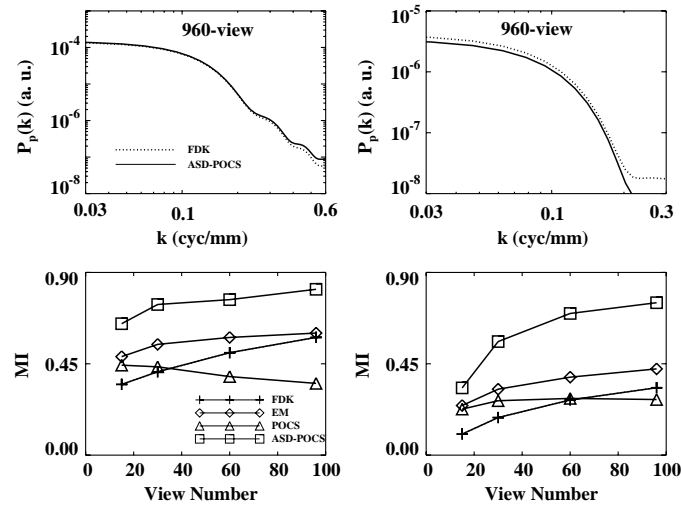


**Figure 18.** Row 1: power spectra computed from the FDK-reference (dotted curve) and ASD-POCS-reference (solid curve) images. Row 2: MIs, as functions of projection views, computed from cylindrical (left) and head (right) phantom images obtained using the FDK (+), EM ( $\diamond$ ), POCS ( $\triangle$ ) and ASD-POCS ( $\square$ ) algorithms and the ASD-POCS-reference image. They differ from their counterparts in figures 5 and 13, which were obtained with the FDK-reference images.

the power spectra of the two reference images show some differences at high frequencies. When the ASD-POCS-reference image is used for computing the similarity-based metrics, evaluation results different from those obtained with the FDK-reference image are expected. As an example, MIs computed using the ASD-POCS-reference images are shown in row 2 of figure 18, and it can be observed that they are considerably higher than their counterparts in figures 5 and 13 obtained with the FDK-reference images.

The results shown bear certain information of spatial resolution in reconstructions. However, some widely used tools such as the modulation transfer function (MTF) for image-resolution evaluation may not be meaningfully defined for the cases under study due not only to gross violations of linearity and shift-invariance but also because an iterative algorithm is based generally on a discrete imaging model in which the system matrix depends on the data-array size and the image-array size. The use of different image-array sizes leads to different system matrices and, consequently, to essentially different optimization problems. Depending upon the selected sizes of an image array and the associated voxels, the optimization problem can become highly under-determined and thus result in distinct reconstructions. Therefore, schemes and metrics for the evaluation of spatial resolution in linear, analytic reconstructions may not simply be applied to nonlinear, iterative reconstructions. Some of the evaluation studies were carried out based upon ROI images within selected 2D slices in 3D reconstructions. We have also performed such evaluation studies in 3D ROI images and obtained evaluation results similar to those described above.

## 8. Discussion

The work focuses on imaging configurations consisting of flat-panel detector and circular scanning trajectory, which are the most widely adopted imaging configurations in non-



diagnostic CT. The ASD-POCS algorithm can readily be applied to imaging configurations of curved or spherical detector and non-circular scanning trajectories such as helical trajectory. There are other issues worthy of future studies, which the ASD-POCS algorithm can also be tailored to tackle. In this study, we considered image reconstruction only from data collected at uniformly distributed sparse views. We investigated an efficient form of ASD-POCS image reconstruction from real data collected in breast tomosynthesis in which the scanning angle ( $\approx 20^\circ$ ) is severely limited (Sidky *et al* 2009). However, CT imaging involving angular ranges of  $100^\circ$ – $180^\circ$  may find a wide variety of applications. Therefore, investigation of image reconstruction from real data collected from such angular ranges should bear considerable practical significance. Furthermore, in the study reported here, the signal-to-noise (SNR) ratios at each view in both sparse-view and full data sets remain comparable. As such, the total radiation dose in a sparse-view data set is only a small fraction of that in the full data set. It is also of practical significance to investigate image reconstruction as a function of the view number, and the SNR level at each view, in real data studies.

A complete iteration in the ASD-POCS algorithm consists of forward/backward projections and image-TV computations and, as such, of more than twice the number of computation operations in the FDK. Therefore, the computation time of the ASD-POCS with  $N$  iterations can be more than  $2N$  times longer than that of the FDK. In contrast, the forward/backward projections within a complete iteration in the ASD-POCS, POCS and EM are comparable, but the ASD-POCS involves additional TV-minimization computations. The computation speed of the ASD-POCS algorithm can be enhanced substantially through streamlining/parallelizing its implementation and/or by exploiting the available, or rapidly available, high performance computational hardware such as multi-core CPU, graphic processing unit (GPU) (Xu and Mueller 2005) and cell engines (Kachelrieß *et al* 2007). Although most of the computation results presented were obtained with more than 100 iterations, depending upon imaging conditions and application tasks, it is possible that images obtained at iteration numbers (e.g.  $\sim 10$ ) much smaller than 100 can be of sufficient practical utility, as evidenced by the visualization-based and quantitative-metrics-based results presented. It is worth pointing out that the ASD-POCS provides a framework for solving a constraint optimization problem. In this study, the POCS-step employs, e.g. the POCS for lowering the data divergence. However, other appropriate algorithms such as the simultaneous algebraic reconstruction technique (SART) (Andersen and Kak 1984) and gradient descent can also be used.

As mentioned above, algorithms different from the EM, POCS and ASD-POCS may be derived for solving the corresponding unconstrained and constrained optimization formulations under consideration. Moreover, one can design different optimization formulations and derive reconstruction algorithms specifically for solving the formulations. These algorithms are worthy of future investigation.

## 9. Conclusion

The current work demonstrates and evaluates the potential and robustness of constrained TV-minimization and the ASD-POCS algorithm in image reconstruction of potential utility from *real* data, collected in CBCT experiments, which contain realistic physical factors that may not be included in simulation studies. To evaluate the multiple facets of image quality, the study consisted of several levels of analysis for revealing different aspects of reconstruction properties, ranging from visual inspection to quantitative-metric-based analysis to detection-task-based assessment. Results of the study demonstrate that, for the imaging conditions, including x-ray flux and data calibration, under consideration, the ASD-POCS algorithm

consistently reconstructs images of quality comparable to that of the FDK-reference image from data that are much less than the full data currently used. These results demonstrate the potential for reconstruction approaches and algorithms, such as the constrained TV-minimization and the associated ASD-POCS algorithm, to yield high image quality at significantly reduced view sampling. The implication for dose reduction suggests a potentially important role for such approaches in the future of CT applications.

## Acknowledgments

This work was supported in part by NIH grants R01CA120540, R01EB000225 and R01CA112163. JB and XH were supported in part by DoD Predoctoral Training grants BC083239 and PC094510, and EYS was also supported in part by a Career Development Award from NIH SPORE grant CA125183-03. Some computation in the work was performed on a cluster partially funded by NIH grants S10RR021039 and P30CA14599. The contents of this paper are solely the responsibility of the authors and do not necessarily represent the official NIH view. The authors would like to thank Mr Tward of Johns Hopkins University for assistance with data collection on the CBCT bench and Dr Reiser of The University of Chicago for valuable discussions of detectability studies. Data were acquired at the previous institution of JHS (Ontario Cancer Institute, University Health Network, Toronto, ON), with gratitude for the expertise and support of collaborators, including Drs Jaffray, Moseley and Paige.

## References

- Andersen A H and Kak A C 1984 Simultaneous algebraic reconstruction technique (SART): a superior implementation of the ART algorithm *Ultrason. Imaging* **6** 81–94
- Brenner D J and Hall E J 2007 Computed tomography—an increasing source of radiation exposure *N. Engl. J. Med.* **357** 2277–84
- Brooks R A, Glover G, Talbert A J, Eisner R L and DiBianca F A 1979 Aliasing: a source of streaks in computed tomograms *J. Comput. Assist. Tomogr.* **3** 511–8
- Barrett H H and Myers K J 2003 *Foundations of Image Science* (New York: Wiley)
- Burgess A E and Judy P F 2007 Signal detection in power-law noise: effect of spectrum exponents *J. Opt. Soc. Am. A* **24** B52–60
- Burgess A E, Jacobson F L and Judy P F 2001 Human observer detection experiments with mammograms and power-law noise *Med. Phys.* **28** 419–37
- Crawford C R and Kak A C 1979 Aliasing artifacts in computerized tomography *Appl. Opt.* **18** 3704–11
- Candès E, Romberg J and Tao T 2006 Robust uncertainty principles: exact signal reconstruction from highly incomplete frequency information *IEEE Trans. Inf. Theory* **52** 489–509
- Candès E, Romberg J and Tao T 2006 Stable signal recovery from incomplete and inaccurate measurements *Commun. Pure Appl. Math.* **59** 1207–23
- Candès E and Wakin M B 2008 An introduction to compressive sampling *IEEE Signal Process Mag.* **25** 21–30
- Combettes P L 1993 The foundations of set theoretic estimation *Proc. IEEE* **81** 182–208
- Chiarot C B, Siewerdsen J H, Haycocks T, Moseley D J and Jaffray D A 2005 An innovative phantom for quantitative and qualitative investigation of advanced X-ray imaging technologies *Phys. Med. Biol.* **50** N287–97
- Delaney A, Bresler Y and Sunnyvale C 1998 Globally convergent edge-preserving regularized reconstruction: an application to limited-angle tomography *IEEE Trans. Image Process.* **7** 204–21
- Dempster A P, Laird N M and Rubin D B 1977 Maximum likelihood from incomplete data via the EM algorithm *J. R. Stat. Soc. Ser. B Stat. Methodol.* **39** 1–38
- Feldkamp L A, Davis L C and Kress J W 1984 Practical cone-beam algorithm *J. Opt. Soc. Am. A* **1** 612–9
- Gonzalez A B De, Mahesh M, Kim K, Bhargavan M, Lewis R, Mettler F and Land C 2009 Projected cancer risks from computed tomographic scans performed in the United States in 2007 *Arch. Intern. Med.* **169** 2071–7
- Galigekere R R, Wiesent K and Holdsworth D W 1999 Techniques to alleviate the effects of view aliasing artifacts in computed tomography *Med. Phys.* **26** 896–904



- Gordon R, Bender R and Herman G T 1970 Algebraic reconstruction techniques (ART) for three-dimensional electron microscopy and X-ray photography *J. Theor. Biol.* **29** 471–81
- Gang G J, Tward D J, Lee J and Siewerdsen J H 2010 Anatomical background and generalized detectability in tomosynthesis and cone-beam CT *Med. Phys.* **37** 1948–65
- Herman G T and Davidi R 2008 Image reconstruction from a small number of projections *Inverse Problems* **24** 045011
- International Commission on Radiation Units and Measurements 1996 Medical image—the assessment of image quality *ICRU Report No 54* (Bethesda, MD: ICRU)
- Katsevich A 2002 Theoretically exact filtered backprojection-type inversion algorithm for spiral CT *SIAM J. Appl. Math.* **62** 2012–26
- Kachelrieß M, Knaup M and Bockenbach O 2007 Hyperfast parallel-beam and cone-beam backprojection using the cell general purpose hardware *Med. Phys.* **34** 1474–86
- La Riviere P J and Pan X 1999 Few-view tomography using roughness-penalized nonparametric regression and periodic spline interpolation *IEEE Trans. Nucl. Sci.* **46** 1121–8
- Loose S and Leszczynski K W 2001 On few-view tomographic reconstruction with megavoltage photon beams *Med. Phys.* **28** 1679–88
- Li M, Yang H and Kudo H 2002 An accurate iterative reconstruction algorithm for sparse objects: application to 3D blood vessel reconstruction from a limited number of projections *Phys. Med. Biol.* **47** 2599–609
- Leng S, Tang J, Zambelli J, Nett B, Tolakanahalli R and Chen G-H 2008 High temporal resolution and streak-free four-dimensional cone-beam computed tomography *Phys. Med. Biol.* **53** 5653–73
- Metheany K G, Abbey C K, Packard N and Boone J M 2008 Characterizing anatomical variability in breast CT images *Med. Phys.* **35** 4685–94
- Pack J D, Noo F and Clackdoyle R 2005 Cone-beam reconstruction using the backprojection of locally filtered projections *IEEE Trans. Med. Imaging* **24** 70–85
- Pan X, Sidky E Y and Vannier M 2009 Why do commercial CT scanners still employ traditional, filtered back-projection for image reconstruction? *Inverse Problems* **25** 123009
- Pluim J P W, Maintz J B A and Viergever M A 2003 Mutual-information-based registration of medical images: a survey *IEEE Trans. Med. Imaging* **22** 986–1004
- Percival D B and Walden A T 1993 *Spectral Analysis for Physical Applications* (New York: Cambridge University Press)
- Reiser I S and Nishikawa R M 2010 Task-based assessment of breast tomosynthesis: effect of acquisition parameters and quantum noise *Med. Phys.* **37** 1591–600
- Smith-Bindman R, Lipson J, Marcus R, Kim K, Mahesh M, Gould R, de Gonzalez A B and Miglioretti D L 2009 Radiation dose associated with common computed tomography examinations and the associated lifetime attributable risk of cancer *Arch. Intern. Med.* **169** 2078–86
- Sidky E Y, Kao K-M and Pan X 2006 Accurate image reconstruction from few-views and limited-angle data in divergent-beam CT *J. X-Ray Sci. and Technol.* **14** 119–39
- Sidky E Y and Pan X 2008 Image reconstruction in circular cone-beam computed tomography by constrained, total-variation minimization *Phys. Med. Biol.* **53** 4777–807
- Sidky E, Anastasio M and Pan X 2010 Image reconstruction exploiting object sparsity in boundary-enhanced X-ray phase-contrast tomography *Opt. Express* **18** 10 404–22
- Shepp L A and Vardi Y 1982 Maximum likelihood reconstruction for emission tomography *IEEE Trans. Med. Imaging* **1** 113–22
- Sidky E Y, Pan X, Reiser I S, Nishikawa R M, Moore R H and Kopans D B 2009 Enhanced imaging of microcalcifications in digital breast tomosynthesis through improved image-reconstruction algorithms *Med. Phys.* **36** 4920–32
- Siewerdsen J H and Jaffray D A 2000 Optimization of X-ray imaging geometry (with specific application to flat-panel cone-beam computed tomography) *Med. Phys.* **27** 1903–14
- Tward D J and Siewerdsen J H 2008 Cascaded systems analysis of the 3D noise transfer characteristics of flat-panel cone-beam CT *Med. Phys.* **35** 5510–29
- Wang Z and Bovik A 2002 A universal image quality index *IEEE Signal Process. Lett.* **9** 81–4
- Xu F and Mueller K 2005 Accelerating popular tomographic reconstruction algorithms on commodity PC graphics hardware *IEEE Trans. Nucl. Sci.* **52** 654–63
- Youla D C and Webb H 1982 Image restoration by the method of convex projections: part 1. Theory *IEEE Trans. Med. Imaging* **1** 81–94
- Zou Y and Pan X 2004 Exact image reconstruction on PI-lines from minimum data in helical cone-beam CT *Phys. Med. Biol.* **49** 941–59

# Investigation of Low-contrast Tumor Detection in Algorithm-enabled Low-dose CBCT

Junguo Bian, *Student Member, IEEE*, Xiao Han, *Student Member, IEEE*, Emil Y. Sidky,  
Jeffrey H. Siewerdsen, and Xiaochuan Pan, *Fellow, IEEE*

**Abstract**—Flat-panel-based X-ray cone-beam computed tomography (CBCT) can provide images of high utility in medical applications such as image-guided surgery and radiotherapy by offering location and contrast information concerning the target and surrounding region. A potential issue in these applications of CBCT is the imaging dose involved because repeated scans are necessary in the image-guided procedures. We investigate algorithm-enabled low-dose CBCT imaging for potential applications to image-guided surgery and radiotherapy procedures, involving detection of low-contrast tumor structures from sparse-view CBCT. Results of our study suggest that images of quality comparable to that of the FDK-reference image can be reconstructed from data much less than full data currently used.

## I. INTRODUCTION

Despite the fact that image quality of flat-panel-based X-ray cone-beam computed tomography (CBCT) is generally inferior to that of advanced diagnostic CT, it can provide images of high utility in medical applications such as image-guided surgery and radiotherapy by offering location and contrast information concerning the target and surrounding region. A issue in these applications of CBCT is the potentially high imaging dose involved often because repeated scans are necessary in the image-guided procedures. one approach to reduce imaging dose is to lower the number of projection views at which data are collected. The use of a lowered number of projection views can also lead to a reduced imaging time in step-and-shoot CBCT, improving workflow, and minimizing potential motion artifacts. However, reducing the number of projection views leads to a challenging image-reconstruction task. The continuous-model-based analytical reconstruction algorithm requires dense sampling of the projection views [1], [2], [3], [4], [5], [6], [7]. When sparse-sampled projection views are used, the analytical algorithms can result in prominent streak artifacts in the reconstruction images. An algorithm, which we referred as adaptive steepest descent-projection onto convex sets (ASD-POCS), has been developed for tackling the sparse-sample reconstruction problem in CBCT through the exploitation of certain prior information such as sparsity of the underlying object function [8], [9], [10]. The ASD-POCS algorithm, which solves the constrained minimization of the image's total variation (TV) subject to a data constraint, has been demonstrated in both simulation studies and real data studies to have a potential for suppressing streak artifacts in CBCT [20], [21].

J. Bian, X Han and E. Y. Sidky are with Departments of Radiology, the University of Chicago.

J. H. Siewerdsen is with Departments of Biomedical Engineering, Johns Hopkins University.

X. Pan is with Departments of Radiology & Cellular Oncology, the University of Chicago.

The work focuses on investigating and evaluating algorithm-enabled low-dose CBCT imaging for potential applications to image-guided surgery and radiotherapy procedures. In particular, we optimize and apply the ASD-POCS algorithm to reconstructing images from real data containing highly sparse views and assess its reconstruction performance in a series of evaluation tasks, including the task of detecting low-contrast tumor structures.

## II. MATERIALS AND METHODS

### A. CBCT System and Physical Phantoms

A bench-top CBCT system, which simulate imaging tasks in image-guided surgery and radiotherapy, was used in the study [11], [12]. The major components of the CBCT system include an X-ray source, a rotatory stage, and a flat-panel detector. The flat-panel detector, with a pitch of 400  $\mu\text{m}$ , has  $1024 \times 1024$  ( $41 \times 41 \text{ cm}^2$ ) elements. A computer-controlled rotation stage is used on which the imaged subject is placed and a circular scanning configuration were used. The distances of the source to the center of rotation and to the detector plane were 93.5 cm and 144.4 cm, respectively. We have performed imaging experiments by using several phantoms, including an anthropomorphic head phantom. The anthropomorphic head phantom was designed for realistically simulating human head [13]. In an attempt to evaluate algorithm performance in detecting low-contrast signals, we have also included several low-contrast structures simulating brain tumors in the head phantom. In each experiment, we have collected *full* data at 960 views over  $2\pi$ . From the full data, we have extracted sparse-view data sets consisting of different number views, including 15, 30, 60 and 96 views, uniformly distributed over  $2\pi$ .

### B. Reconstruction Algorithms

We have assumed that the imaging model in CBCT is a discrete linear system. The ASD-POCS algorithm was developed for image reconstruction that is to solve an optimization problem in which the image total-variation (TV) is minimized subject to the data constraint and image positivity. This algorithm consists of alternating steep-descent (SD) step and projection-onto-convex-set (POCS) step that minimize the image TV and data divergence, respectively. The relative strengths of SD and POCS steps are adaptively adjusted so that the final image is moving toward minimum TV image under the data and other constraints. The ASD-POCS algorithm has been evaluated extensively in simulation studies. In this work, we focus on its modification, application, and evaluation by using real data collected with the CBCT system. For comparison, we have also carried out image reconstruction from the same data by

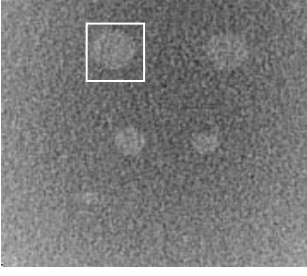


Figure 1. ROI image of the anthropomorphic head phantom within a transverse slice at  $z = -1.0$  cm. The region enclosed by the square in the image indicates one of the low contrast, extended tumors contained in the head phantom. An evaluation study presented here focuses on comparing the model-observer performance based upon images reconstructed by use of the FDK, POCS, and ASD-POCS algorithms in a task of detecting such low-contrast tumor signals.

using the FDK, and POCS [14], [15], [16] algorithms. The POCS algorithm solves an unconstrained minimization problem in which the object function is the Euclidean-data divergence when the data is consistent.

### C. Image Quality Evaluation

We have carried out extensive evaluation of reconstruction quality obtained by using the FDK, POCS, and ASD-POCS algorithms from full and sparse-view data. Our evaluation includes three levels of evaluation. In addition to careful assessment through visual inspection, we also evaluate image reconstruction by using quantitative metrics and task-specific evaluation metric using model observer detectability.

Because there is no ground truth about the phantom for real data studies and because FDK is the most popularly used reconstruction algorithm in various dedicated CT, we use image reconstructed from full data by use of the FDK algorithm as a surrogate truth. We evaluated quantitatively the reconstruction quality by considering Pearson correlation coefficient (PCC) and mean square error (MSE), which can be used for measuring the degree of similarity between the reconstructed and FDK-reference images. The higher the PCC or the smaller the MSE, the more similar the image is to the reference image.

Furthermore, we have conducted evaluation studies on the algorithm performance, in terms of model-observer detectability, in tasks of detecting low-contrast tumor structures. The low-contrast signal involved in the study is shown in Fig. 1. This model observer becomes the so-called ideal observer under the conditions that a linear shift-invariant system is considered, that the image contains uncorrelated Gaussian noise, and that the signal and background are known exactly. Although the conditions cannot be satisfied precisely for images reconstructed from real CBCT data, this model observer has been used as a useful index for yielding approximate evaluation information indicative of algorithms' reconstruction performance in detection tasks [17], [18], [19]. The signal is chose to be low-contrast tumor in the head phantom. The background is subtracted from the signal and the signal is extracted using a mask. We select many square-shaped region of interests (ROIs) of equal size at different locations within the image to calculate the background power spectra. Each of the ROIs is within the support of the entire image and in the homogeneous region of the image. For

detail calculations of the detectability, please refer to our recent published paper [20].

## III. RESULTS

We have carried out image reconstruction for different phantom experiments and evaluation studies of algorithm performance in terms of careful visual inspection, quantitative-metrics-based analysis, and detection-task-based assessment. In this paper, we include a portion of the results related to the head-phantom experiment and more detailed results can be found in our recent paper [20]. An extensive imaging experiments and image quality evaluations using a micro-CT system can also be found in reference [21]. We show in Fig. 2 ROI images of the head phantom within a transverse slice at  $z = -1.0$  cm containing low-contrast objects reconstructed from 60- and 96-view data sets by use of the FDK, POCS, and ASD-POCS algorithms, respectively. We use the FDK-reference image, which is shown in column 3 of Fig. 2, as the reference, because this is the image used currently in CBCT applications. It can be observed that both 60-view and 96-view FDK-reconstruction images are contaminated by streak artifacts, which prevent the low-contrast structures from being discerned, that the low-contrast structures in images reconstructed by use of the POCS algorithm appear to be overwhelmed by the noisy background, and that it is difficult to identify the low-contrast structure reliably. However, images reconstructed from the sparse-view data by use of the ASD-POCS algorithm appear to be similar to the reference image, and the low-contrast structures can be clearly observed in the ASD-POCS images. We also displayed the difference images with respect to the FDK-reference image in Fig. 3. It can be observed that the images reconstructed by use of ASD-POCS algorithm are the closest to the reference image.

In additional to the visual qualitative evaluation, we also computed the PCC and MSE from the reconstruction images of head phantom. We show in Figs 4 and 5 MSE and PCC calculated from the head phantom reconstruction images. It can be observed that ASD-POCS algorithm have smaller MSE and higher PCC comparing with POCS and FDK algorithms. It can also be observed that the performance of FDK is more affected by the number of views.

Furthermore, we also computed the model-observer detectability, in which the task is to detect the low-contrast structure, as illustrated in Fig. 1, for images of the head phantom reconstructed from these sparse-view data sets by use of the FDK, POCS, and ASD-POCS algorithms. In Fig. 6, we display the detectability as functions of projection views calculated from images reconstructed from 15-, 30-, 60-, and 96-view data sets by use of the FDK, POCS, and ASD-POCS algorithms, respectively. The result clearly indicates that the ASD-POCS algorithm yields a detectability higher than do other algorithms under study.

We would also like to point out that FDK-reference image is not the real truth and the use of different reference images in the computation of image-similarity metrics can lead to quantitatively different evaluation result. The use of FDK-reference image generally is in favor of the images reconstructed by use of FDK algorithm.

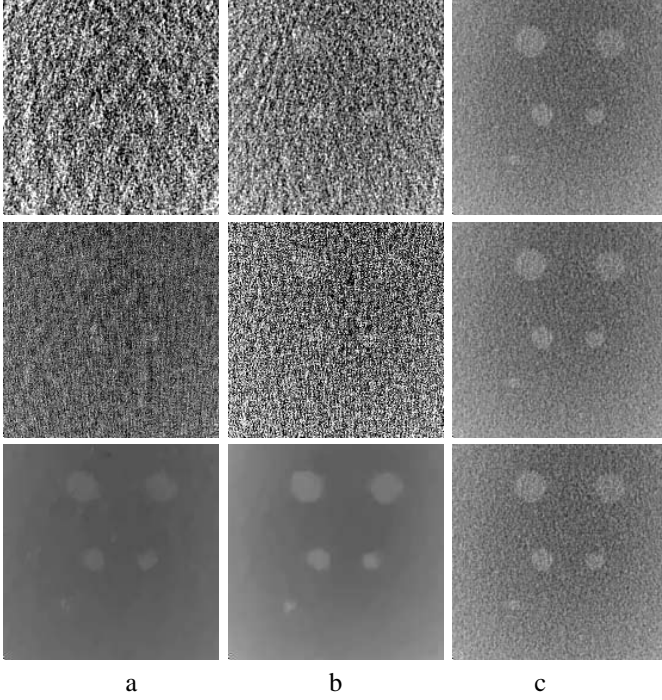


Figure 2. ROI images of the head phantom within a transverse slice at  $z = -1.0$  cm reconstructed from data sets containing (a) 60- and (b) 96-view data sets by use of the FDK (row 1), POCS (row 2), and ASD-POCS (row 3) algorithms. For comparison, we show in column 3 the reference image reconstructed by use of the FDK algorithm from the full 960-view data. The display grey scale is  $[0.1, 0.25] \text{ cm}^{-1}$ .

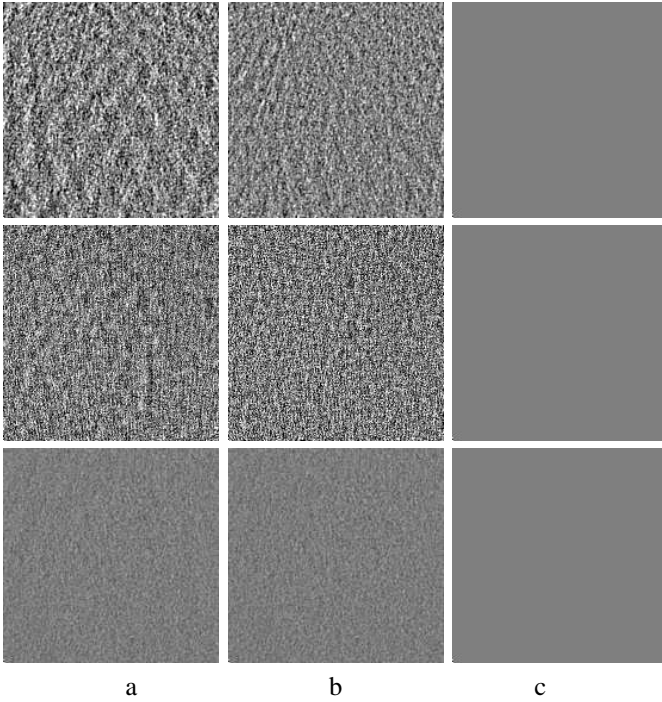


Figure 3. Difference images of the head phantom with respect to the FDK-reference image within ROI in a transverse slice at  $z = -1.0$  cm reconstructed from data sets containing (a) 60- and (b) 96-view data sets by use of the FDK (row 1), POCS (row 2), and ASD-POCS (row 3) algorithms. For comparison, we show in column 3 the reference difference image with all pixel values equals to zero. The display grey scale is  $[-0.05, 0.05] \text{ cm}^{-1}$ .

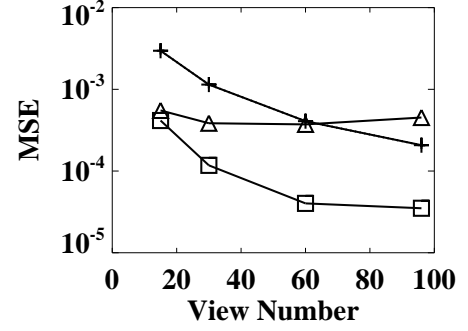


Figure 4. MSE, as a function of projection views, computed from the head phantom images reconstructed by use of the FDK (+), POCS (△), and ASD-POCS (□) algorithms using FDK-reference image.

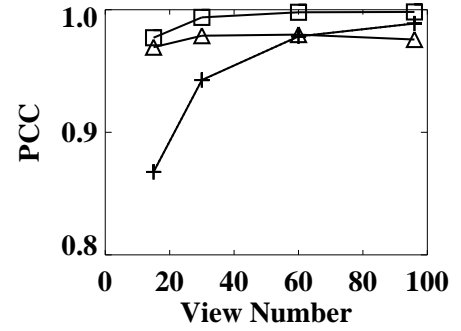


Figure 5. PCC, as a function of projection views, computed from the head phantom images reconstructed by use of the FDK (+), POCS (△), and ASD-POCS (□) algorithms using FDK-reference image.

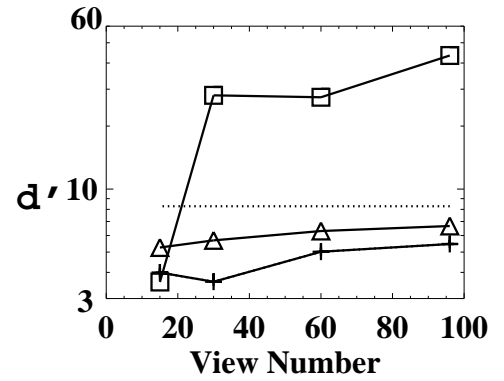


Figure 6. Detectability of the low-contrast tumor structure, as a function of projection views, calculated based upon images reconstructed by use of the FDK (+), POCS (△), and ASD-POCS (□) algorithms. The detectability of the FDK-reference image is plotted as dotted lines.

#### IV. DISCUSSION

We have demonstrated and evaluated the potential and robustness of the ASD-POCS algorithm in image reconstruction of practical utility from real, sparse-view CBCT data. Our study was designed to consist of several levels of analysis for revealing different aspects of reconstruction properties, ranging from visual inspection to qualitative-metric-based analysis to detection-task-based assessment. Results of evaluation analysis, especially in detection-task-based studies, suggest that the ASD-POCS algorithm consistently reconstructed images of quality comparable to that of the FDK-reference image from data much less than full data currently used.

#### REFERENCES

- [1] L. A. Feldkamp, L. C. Davis, and J. W. Kress, "Practical cone-beam algorithm," *J. Opt. Soc. Am. A*, vol. 1, pp. 612–619, 1984.
- [2] F. Noo, M. Defrise, R. Clackdoyle, and H. Kudo, "Single-slice rebinning for helical cone-beam CT," *Phys. Med. Biol.*, vol. 44, pp. 561–570, 1999.
- [3] M. Kachelrieß, S. Schaller, and W. Kalender, "Advanced single-slice rebinning in cone-beam spiral CT," *Med. Phys.*, vol. 27, pp. 754–772, 2000.
- [4] H. Turbell, "Cone-beam reconstruction using filtered backprojection," Ph.D. dissertation, Linköping University, 2001.
- [5] A. Katsevich, "Theoretically exact filtered backprojection-type inversion algorithm for spiral CT," *SIAM J. Appl. Math.*, vol. 62, pp. 2012–2026, 2002.
- [6] Y. Zou and X. Pan, "Exact image reconstruction on PI-lines from minimum data in helical cone-beam CT," *Phys. Med. Biol.*, vol. 49, pp. 941–959, 2004.
- [7] J. D. Pack, F. Noo, and R. Clackdoyle, "Cone-beam reconstruction using the backprojection of locally filtered projections," *IEEE Trans. Med. Imag.*, vol. 24, pp. 70–85, 2005.
- [8] E. Y. Sidky, K.-M. Kao, and X. Pan, "Accurate image reconstruction from few-views and limited-angle data in divergent-beam CT," *J. X-Ray Sci. and Technol.*, vol. 14, pp. 119–139, 2006.
- [9] E. Y. Sidky and X. Pan, "Image reconstruction in circular cone-beam computed tomography by constrained, total-variation minimization," *Phys. Med. Biol.*, vol. 53, pp. 4777–4807, 2008.
- [10] X. Pan, E. Y. Sidky, and M. Vannier, "Why do commercial CT scanners still employ traditional, filtered back-projection for image reconstruction?" *Inverse Probl.*, vol. 25, p. 123009, 2009.
- [11] S. Richard and J. H. Siewerdsen, "Cascaded systems analysis of noise reduction algorithms in dual-energy imaging," *Med. Phys.*, vol. 35, pp. 586–601, 2008.
- [12] —, "Comparison of model and human observer performance for detection and discrimination tasks using dual-energy X-ray images," *Med. Phys.*, vol. 35, p. 5043, 2008.
- [13] C. B. Chiarot, J. H. Siewerdsen, T. Haycocks, D. J. Moseley, and D. A. Jaffray, "An innovative phantom for quantitative and qualitative investigation of advanced X-ray imaging technologies," *Phys. Med. Biol.*, vol. 50, pp. N287–N297, 2005.
- [14] R. Gordon, R. Bender, and G. T. Herman, "Algebraic reconstruction techniques (ART) for three-dimensional electron microscopy and X-ray photography," *J. Theor. Biol.*, vol. 29, pp. 471–481, 1970.
- [15] D. C. Youla and H. Webb, "Image restoration by the method of convex projections: Part 1 – theory," *IEEE Trans. Med. Imag.*, vol. 1, pp. 81–94, 1982.
- [16] P. L. Combettes, "The foundations of set theoretic estimation," in *Proc. IEEE*, vol. 81, 1993, pp. 182–208.
- [17] J. H. Siewerdsen and D. A. Jaffray, "Optimization of X-ray imaging geometry (with specific application to flat-panel cone-beam computed tomography)," *Med. Phys.*, vol. 27, pp. 1903–1914, 2000.
- [18] G. J. Gang, D. J. Tward, J. Lee, and J. H. Siewerdsen, "Anatomical background and generalized detectability in tomosynthesis and cone-beam CT," *Med. Phys.*, vol. 37, pp. 1948–1965, 2010.
- [19] I. S. Reiser and R. M. Nishikawa, "Task-based assessment of breast tomosynthesis: Effect of acquisition parameters and quantum noise," *Med. Phys.*, vol. 37, pp. 1591–1600, 2010.
- [20] J. Bian, J. H. Siewerdsen, X. Han, E. Y. Sidky, J. L. Prince, C. A. Pelizzari, and X. Pan, "Evaluation of sparse-view reconstruction from flat-panel-detector cone-beam CT," *Phys. Med. Biol.*, vol. 55, pp. 6575–6599, 2010.
- [21] X. Han, J. Bian, D. Eaker, T. Kline, E. Sidky, E. L. Ritman, and X. Pan, "Algorithm-enabled low-dose micro-CT imaging," *IEEE Trans. Med. Imag.*, p. in press, 2010.